Development of a track level thermomechanical model for LPBF with a novel approach for plasticity computation

Khuldoon Usman[a], Markus Niessen[b], Wolfgang Schulz[a], and Christian Hinke[c]

[a]Chair of Nonlinear Dynamics for Laser Manufacturing Processes, RWTH Aachen University, Steinbachstrasse 15, 52074 Aachen, Germany
[b]Fraunhofer Institute for Laser Technology, Steinbachstrasse 15, 52074, Aachen, Germany
[c]Chair of Laser Technology, RWTH Aachen University, Steinbachstrasse 15, 52074 Aachen, Germany

ABSTRACT

The Laser Powder Bed Fusion (LPBF) process is characterized by rapid thermal cycles that induce complex thermo-mechanical phenomena such as significant plastic strain accumulation and residual stress formation. Simulation models for the process are gaining popularity due to the limitations of experimental techniques but are often extensive and computationally demanding, limiting their practical application for process optimization. In this study, a thermo-elastoplastic model for simulating the LPBF process at the track level is developed. The model uses a moving Goldak heat source along with temperature-dependent material properties and phase changes to accurately capture transient thermal distributions and is coupled with an elastoplastic model. The model strives for an effective balance between efficiency and accuracy and is compared with other experimentally validated simulation models. A key contribution of this study is the comparative analysis of numerical strategies for plasticity. A conventional fully consistent implicit Newton solver for the nonlinear mechanical problem, is compared against a Quasi-Newton fixed point approach, where nonlinear terms of the tangent stiffness matrix are relocated to the right-hand side of the weak form and treated explicitly. This formulation is designed to maintain accuracy while offering improved computational efficiency. Preliminary runs on simple elastoplastic models in the past have shown good computational improvements by reducing calculation times thus simplifying the computational cost of plastic fidelity.

Keywords: simulations, additive manufacturing, thermomechanical, plastic deformations

1. INTRODUCTION

The Laser Powder Bed Fusion (LPBF) has emerged as a feasible and flexible alternative to classical manufacturing techniques for the manufacturing of complex parts with a variety of features and structures.[1,2] This technique focuses on building a part through the selective heating and cooling of individual layers of powder material and upon solidification, the sequential joining of these layers forms the final component in an *additive* manner. In this way, it is a cost effective manufacturing strategy in terms of material waste as well as minimzation of processing steps.[3] Nevertheless, the LPBF process has its challenges due to the use of an extermely focused energy source –

Further author information: (Send correspondence to K. Usman)
E-mail: khuldoon.usman@nld.rwth-aachen.de, Telephone: +49 241 80 40429
W. Schulz is now a retired guest professor at the Chair of Nonlinear Dynamics for Laser Manufacturing Processes

This is the accepted manuscript of the following article: Khuldoon Usman, Markus Niessen, Wolfgang Schulz, and Christian Hinke "Development of a track level thermomechanical model for LPBF with a novel approach for plasticity computation", Proc. SPIE 13884, Laser 3D Manufacturing XIII, 138840A (5 March 2026); https://doi.org/10.1117/12.3070776.

laser beam – to process the material.[4,5] The large amounts of energy deposition lead to extermely large temperature gradients which lead to unwanted build up of residual stresses and post-manufacturing distortion.[6] These large temperatures also limit the feasibility of experimental techniques that can be performed to measure these temperatures, especially in the near field of the laser beam or molten material region, known as the meltpool.[7,8] Thus, to improve understanding of the process, for analysis and better process control, simulations of the LPBF process serve considerable benefit in being able to recreate the process conditions and thus trying to model and predict the thermal and mechanical deformation during the process. These simulations are considerably complex and require suitable approximations and modelling strategies to make them physically valid and computationally feasible simulateneously.[9,10] Therefore, considerable research as been invested in building accurate models of the LPBF process that can also be executed in reasonable timeframes. However, many simulations are conducted on commercial Finite Element Method (FEM) software which are not only costly but also are limited in terms of what flexibilities can be implemented, when compared to fully open-source, programmable models.[11–13]

Earlier models have been developed primarily for the thermal computations of the process. These models study the process at different length and time scales to investigate various phenomena, and have varying levels of complexity to make the approach both computationally feasible and accurate.[10,14] Some of these models focused on approximating the shape of the heat source that generates the energy deposition of the laser beam.[15] Further approximations of the energy deposition were necessary to demand feasible computation times of models at the part level or multiple layers.[16] Also, there are models that assume constant or temperature-independent properties which affect accurate computations of meltpool shapes and temperature distribution, especially in the regions of high temperature gradients. These approximations sometimes lead to deficiencies in the overall modelling of the thermal evolution, to make the computation feasible. Most of the eariler models were limited to just the temperature simulation and did not model mechanical deformation to better evaluate the build up of stresses inside the part.

Recently, more and more studies have investigated full thermomechanical modelling of the process to better understand stress and strain build up but they are also only feasible when running mechanical models for a few layers or small test parts.[15] This is because even though track level modelling of the temperatures can still be feasibly achieved with current hardware, a full part level simulation with all of the microscale aspects (at the scale of laser beam) takes unreasonably large times to compute, especially for desktop computers.[10,14,17] Large High Performance Compute (HPCs) Clusters are needed for such a full simulation. Thus, it is difficult to find models that study both thermal and mechanical deformation at the scale of multiple tracks. However, these models are also essential since track level models can highlight the necessity for keeping track of plastic strain evolution on the microscale due to areas of high stress left over from many heating and cooling cycles in non-overlapping regions of the laser beam.[17,18] This leads to embedded plastic strains that can accumulate over time as more and more tracks are scanned and whole hatches and layers accumulate. To resolve this issue, some researchers have used the inherent strain method, to approximate plastic strain evolution for full part level simulations by modelling a *pre-stressed* part with plastic strains (extracted from track or hatch level models), however they are usually constant/averaged for the whole duration of the simulation and do not model the plastic strains as a true distribution generated by multiple tracks overlapping with each other.[17–20] Tangestani *et al.* have proposed a track level model to keep track of local stresses and plasticity variations using a *Hybrid-Line* heat source but that model is also very computationaly complex and thus requires several hours to solve for a single track.[21] Consequently, very few full thermomechanical models for the track level simulation of LPBF are published especially those that can achieve a suitable balance between accuracy (of local stress and strain history) and computational feasibility, thus limiting the effectiveness at which information can be transferred to a larger scale.

The focus of this work is to build a robust and effective thermomechanical model for the LPBF process that is also computationally efficient. Thus, the model will have two main parts. The first part, for the thermal calculation will focus on solving the heat conduction equation with temperature-dependent material properties and a parametric heat source to effectively model a physical valid temperature distribution that represents the moving laser beam and associated meltpool for multiple laser beam scan paths/tracks. This will then be coupled to a mechanical model in small enough increments to keep track of the associated mechanical deformation due to the thermal strain. The mechanical model will track the overall plastic deformation by using the input thermal strains as mechanical loading for the overall nonlinear problem. For each iteration of the nonlinear problem,

a constitutive model will be solved in conjuction with an appropriate return mapping approach should plastic deformation occur. The full model will then be studied on a thermomechanical benchmark problem. The model will also be compared with other relevant thermal models which have already been experimentally validated and subsequently, an overall computational performance analysis of the model will be presented. The eventual goal is to then have a model that can be easily scaled up to different length and time scales such as the patch/hatch level and even more so on the modelling of multiple layers. As this model is implemented using open-source libraries in the Python language, it is completely open-source and flexible due to modularity. It allows for additional complexities to be introduced and can take advantage of cutting-edge computational speedup approaches that have not yet been incorporated into commerical FEM software.

Due to the nature of the problem, especially for larger geometries and meshes, the mechanical problem can be far more computationally demanding than the thermal problem. Thus, one additional aspect of this research is the implementation and investigation of an *explicit* approach for solving the nonlinear mechanical weak form. The goal of this approach would focus on being able to simplify the bilinear form/stiffness matrix on the left hand side, so that it must not be assembled and reinverted in every iteration of the problem and the nonlinear (plasticity) terms can be incorporated explicitly into the linear form on the right hand side, essentially treating this as a *fixed-point* problem. Preliminary runs have shown this is significantly faster per iteration and shows potential for overall improvement in computational time compared to the classical approach.

2. GOVERNING EQUATIONS

A combined thermomechanical model first begins with the partial differential equations of heat conduction and solid elasticity. These are the *strong forms* of the problem that are represented in a purely continuum sense. The heat conduction problem models temperature variation in both time and space and thus must be solved with suitable boundary and initial conditions i.e., an Initial Boundary Value Problem (IBVP) whereas the mechanical problem is a problem of elastoplasticity defined for displacement, stress and plastic strains over the spatial domain for predefined timesteps of the thermal problem, its loading stems from thermal strains generated by the temperature variation. Solving the strong forms is implemented via spatial discretization techniques such as the Finite Element Method (FEM) by first converting the strong form into a *weak form* which represent the thermal and mechanical problem in a variational sense over the entire domain. These weak forms are then used to incorporate boundary conditions as well time discretization of the problem. They can then be assembled into matrix vector systems (system of algebraic equations) which can be solved via commercial FEM programs or open source FEM implementations.

2.1 Strong form - Thermal

For the thermal problem, the first step is to begin with the three dimensional heat equation that solves for the temperature T for a given time t and position $\mathbf{x} = (x, y, z)$ in a domain Ω such that

$$\rho(T)c_p(T)\frac{\partial T(\mathbf{x},t)}{\partial t} - \nabla \cdot (k(T)\nabla T(\mathbf{x},t)) = Q(\mathbf{x},t) \quad \text{in } \Omega \times (0, t_{\text{final}}) \ , \tag{1}$$

where $\rho(T)$ is the density, $c_p(T)$ is the specific heat capacity, $k(T)$ is the thermal conductivity, and $Q(\mathbf{x}, t)$ is a volumetric heat source term representing a moving laser. The domain is assumed to be sufficiently large enough such that surface boundaries far away from the heat source can be modelled with a general convection boundary condition. However, the surface upon which the laser beam is incident Γ_l, needs to be modelled with a suitable radiation boundary condition due to the larger temperature gradients. The base of the domain (bottom surface) Γ_b is in this case assumed to be considerably far away from the heat source such that it can be considered clamped at T_0 during the movement of the laser beam. Thus, the boundary conditions are

$$\begin{aligned} -k(T)\nabla T \cdot \mathbf{n} &= \sigma\epsilon(T^4 - T_0^4) && \text{on } \Gamma_l \ , \\ T &= T_0 && \text{on } \Gamma_b \ , \\ -k(T)\nabla T \cdot \mathbf{n} &= h(T - T_0) && \text{on } \partial\Omega \setminus (\Gamma_l \cup \Gamma_b) \ , \end{aligned} \tag{2}$$

The initial condition over the entire domain is

$$T(\mathbf{x}, 0) = T_0 \quad \text{in } \Omega \ , \tag{3}$$

where T_0 is the room (ambient) temperature, h is the convection coefficient, ϵ is the emissivity and σ is the Stefan-Boltzmann constant. The convection boundary condition is physically justified, if the boundaries are sufficient characteristic diffusion lengths away from the laser spot.[22–24] A common choice for the source function that simulates a moving laser in LPBF is a 3D Gaussian distribution[25,26]

$$Q(\mathbf{x}, t) = \frac{3\sqrt{3}\eta P}{\pi^{3/2} r^2 d} \exp\left(-\frac{3(x - x_0(t))^2}{r^2} - \frac{3(y - y_0(t))^2}{r^2} - \frac{3(z - z_0(t))^2}{d^2} \right) \ , \tag{4}$$

where η is laser absorption efficiency, P is laser power, r is the radial spread of the distribution (usually laser beam radius), d is the depth of the heat source, and $(x_0(t), y_0(t), z_0(t))$ is the moving center of the heat source. However, Goldak *et. al.* showed that the Gaussian source underestimates the penetration depth of the heat for very high power density sources, such as a laser beam, which is why they suggested replacing it with a hemispherical model which did overcome this challenge but did not approximate the meltpool geometry well. They finally proposed a double ellipsoidal model to better overcome these limitations and to improve the temperature gradients approximated from previous models.[27] A detailed expression of this heat source is elaborated in Sec 4.1.

2.2 Strong form - Mechanical

After solving the thermal problem, the thermal strains are computed from the temperature field to be used for the mechanical part of the problem. The strong form of a problem in elasticity is

$$\nabla \cdot \boldsymbol{\sigma}(\mathbf{x}) + \mathbf{b}(\mathbf{x}) = \mathbf{0} \quad \text{in } \Omega \ , \tag{5}$$

where $\boldsymbol{\sigma}$ is the Cauchy stress tensor and $\mathbf{b}$ is the body force per unit volume. For a rectangular domain $\Omega = [0, L_x] \times [0, L_y] \times [0, L_z]$, the dirichlet boundary conditions are applied on the displacement $\mathbf{u}$ to constraint the bottom end of the domain

$$\mathbf{u}(\mathbf{x}) = \mathbf{0} \quad \text{on } \Gamma_D = \{\mathbf{x} \in \partial\Omega \mid z = 0\} \ , \tag{6}$$

while the Neumann boundary condition is enforced as a zero traction boundary condition on all other boundaries

$$\boldsymbol{\sigma} \cdot \mathbf{n} = \mathbf{0} \quad \text{on } \Gamma_N = \partial\Omega \setminus \Gamma_D \ , \tag{7}$$

where $\mathbf{n}$ is the outward unit normal to the boundary. The stress tensor $\boldsymbol{\sigma}$ is computed from the constitutive tensor $\mathbb{C}$ (assumed isotropic material) and the elastic part of the total strain tensor

$$\boldsymbol{\sigma} = \mathbb{C} : \left(\boldsymbol{\varepsilon} - \boldsymbol{\varepsilon}^p - \boldsymbol{\varepsilon}^{\text{th}}\right) = \lambda \, \text{tr}(\boldsymbol{\varepsilon} - \boldsymbol{\varepsilon}^p - \boldsymbol{\varepsilon}^{th})\mathbf{I} + 2\mu(\boldsymbol{\varepsilon} - \boldsymbol{\varepsilon}^p - \boldsymbol{\varepsilon}^{th}) \ , \tag{8}$$

where $\boldsymbol{\varepsilon} = \frac{1}{2}(\nabla \mathbf{u} + \nabla \mathbf{u}^\top)$ is the total strain, $\boldsymbol{\varepsilon}^{\text{th}} = \alpha(T - T_0)\mathbf{I}$ is the thermal strain and $\boldsymbol{\varepsilon}^p$ represents the plastic strain. $\lambda = \frac{E\nu}{(1+\nu)(1-2\nu)}$ and $\mu = \frac{E}{2(1+\nu)}$ are the First and Second Lamé parameters respectively. Additionally, α is the coefficient of thermal expansion, T_0 is the initial temperature and E and ν are the Young's Modulus and Poisson's ratio, respectively.

To compute the plastic strain tensor $\boldsymbol{\varepsilon}^p$, a yield criterion for the stress has to be defined. In this work, the von Mises yield criterion with isotropic hardening (using the J2 flow rule) is used[28]

$$f(\boldsymbol{\sigma}, p) = \sqrt{\frac{3}{2}\boldsymbol{s} : \boldsymbol{s}} - \sigma_y(p) \leq 0 \ , \tag{9}$$

where

- $\boldsymbol{s} = \boldsymbol{\sigma} - \frac{1}{3}\text{tr}(\boldsymbol{\sigma})\mathbf{I}$ is the deviatoric part of the stress tensor,

- $\sigma_y(p) = \sigma_{y0} + Hp$ is the temperature-dependent yield stress with linear isotropic hardening parameter H,
- and p is the accumulated plastic strain.

The associated flow rule for the yield criterion is

$$\dot{\boldsymbol{\varepsilon}}^p = \dot{\lambda}\frac{\partial f}{\partial \boldsymbol{\sigma}} = \dot{\lambda}\frac{3}{2}\frac{\boldsymbol{s}}{\sqrt{\frac{3}{2}\boldsymbol{s}:\boldsymbol{s}}}\ , \tag{10}$$

with consistency condition $\dot{\lambda} \geq 0$, $f \leq 0$, $\dot{\lambda} f = 0$ and the accumulated plastic strain rate is

$$\dot{p} = \sqrt{\frac{2}{3}\dot{\boldsymbol{\varepsilon}}^p : \dot{\boldsymbol{\varepsilon}}^p}. \tag{11}$$

The term $\frac{\partial f}{\partial \boldsymbol{\sigma}}$ represents the normal to the convex yield surface. Further simplification yields

$$\frac{\partial f}{\partial \boldsymbol{\sigma}} = \frac{\partial f}{\partial \boldsymbol{\sigma}_{ij}} = \frac{\partial \sigma_{eq}}{\partial \boldsymbol{\sigma}_{ij}} = \frac{3}{2}\frac{\boldsymbol{s}}{\sigma_{eq}}\ , \tag{12}$$

where $\sigma_{eq} = \sqrt{\frac{3}{2}\boldsymbol{s}:\boldsymbol{s}}$. Substituting the expression for $\dot{\boldsymbol{\varepsilon}}^p$ in Eq. (10) into Eq. (11)

$$\dot{p} = \sqrt{\frac{2}{3}\dot{\boldsymbol{\varepsilon}}^p : \dot{\boldsymbol{\varepsilon}}^p} = \sqrt{\frac{2}{3}\left(\dot{\lambda}\frac{\partial f}{\partial \boldsymbol{\sigma}}\right) : \left(\dot{\lambda}\frac{\partial f}{\partial \boldsymbol{\sigma}}\right)} = \sqrt{\frac{2}{3}\left(\dot{\lambda}\frac{3}{2}\frac{\boldsymbol{s}}{\sigma_{eq}}\right) : \left(\dot{\lambda}\frac{3}{2}\frac{\boldsymbol{s}}{\sigma_{eq}}\right)} = \dot{\lambda}\sqrt{\frac{3}{2}\frac{\boldsymbol{s}:\boldsymbol{s}}{\sigma_{eq}^2}} = \dot{\lambda}\sqrt{\frac{3}{2}\frac{\boldsymbol{s}:\boldsymbol{s}}{\frac{3(\boldsymbol{s}:\boldsymbol{s})}{2}}} = \dot{\lambda}. \tag{13}$$

Thus, Equation (10) can be reformulated to show that $\dot{\boldsymbol{\varepsilon}}^p = \dot{p}\frac{3}{2\sigma_{eq}}\boldsymbol{s}$. The flow theory of plasticity states, that these equations are modelled as rate equations to model evolution of plastic deformation. Thus, analogous to time dependent problems, the algorithmic implementation requires solving the mechanical problem in incremental form to ensure stability of the solver, essentially an *incremental integration* algorithm over a *pseudo-time*.[29,30] Further discussion of the implementation of this algorithm is done in Sec. 3.

2.3 Weak form - thermal

For solving the heat conduction, the weak form is needed to implement the FEM. A test function $v \in V$ is multiplied by the strong form and integrated over the domain Ω, and then applying integration by parts leads to

$$\int_\Omega \rho c_p \frac{\partial T}{\partial t} v\, dV + \int_\Omega k(T)\nabla T \cdot \nabla v\, dV + \int_{\partial\Omega\setminus\Gamma_l} h(T - T_0)v\, dS + \int_{\Gamma_l} \sigma\epsilon(T^4 - T_0^4)v\, dS = \int_\Omega Q(\mathbf{x}, t)v\, dV\ , \tag{14}$$

where V is the space of test functions (e.g., $H^1(\Omega)$).[31] The Neumann radiation and convection boundary appear naturally, as surface integrals, but the Dirichlet boundary condition will be explicitly enforced (when this form is assembled into a matrix). The trial function in the radiation boundary condition makes the weak form nonlinear. The radiation term contains higher order terms of the trial function i.e. $(T)^4$ which is computationally not possible for a linear problem in FEM since basis functions usually belong to the function space of polynomials with maximum C^0 continuity i.e., $T, v \in H^1(\Omega)$. This requires solving a nonlinear problem, or using complex function spaces, which is computationally challenging. To circumvent this, the radiation boundary condition can be replaced with a convection term with a heat transfer coefficient h_{rad} that is usually orders of magnitude higher than the normal convection coefficient i.e., $h_{rad} \gg h$. This modifies the radiation boundary condition, which can now be modelled as an *approximate* convection boundary condition[32]

$$\int_\Omega \rho c_p \frac{\partial T}{\partial t} v\, dV + \int_\Omega k(T)\nabla T \cdot \nabla v\, dV + \int_{\partial\Omega\setminus(\Gamma_l\cup\Gamma_b)} h(T - T_0)v\, dS + \int_{\Gamma_l} h_{rad}(T - T_0)v\, dS = \int_\Omega Q(\mathbf{x}, t)v\, dV\ . \tag{15}$$

This better approximates the higher temperature gradients and the higher heat loss due to radiation at the laser beam surface Γ_l. It also allows for the radiation boundary condition to be represented with a T term of linear order which can be approximated by standard linear FEM basis functions. The weak form in Eq. (15) is the basis of the time dependent heat transfer problem which will be solved with relevant time-stepping schemes in the computational approach. For one or more timesteps, the change in temperature distribution i.e., *thermal increment*, will be the source of incremental loading/strain for the mechanical problem i.e, a weakly coupled thermomechanical problem.

2.4 Weak form - mechanical

In the mechanical problem, for a given number of thermal increment(s)/step(s), a nonlinear problem needs to be solved for the displacement $\mathbf{u}$ because the plastic deformation creates a nonlinear stress-strain relation. Thus, the problem must be formulated in the form of a linearized equlibrium balance, i.e., residual (to use Newton's method) before it can be discretized. Integrating a test function $\mathbf{w}$ with the strong form, it can be shown that

$$\int_\Omega \mathbf{w} \cdot (\nabla \boldsymbol{\sigma} + \mathbf{b})\, dV = 0 \ . \tag{16}$$

Integrating the divergence term by parts (and vanishing zero traction boundary condition terms) and rearranging leads to

$$\mathcal{R}(\mathbf{u}) = \int_\Omega \nabla \mathbf{w} : \boldsymbol{\sigma}(\mathbf{u})\, dV - \int_\Omega \mathbf{w} \cdot \mathbf{b}\, dV = 0 \ . \tag{17}$$

Substituting $\boldsymbol{\sigma}(\mathbf{u}) = \mathbb{C} : \big(\boldsymbol{\varepsilon}(\mathbf{u}) - \boldsymbol{\varepsilon}^{\text{th}} - \boldsymbol{\varepsilon}^{p}\big)$ gives

$$\mathcal{R}(\mathbf{u}) = \int_\Omega \nabla \mathbf{w} : \Big[\mathbb{C} : (\boldsymbol{\varepsilon}(\mathbf{u}) - \boldsymbol{\varepsilon}^{\text{th}} - \boldsymbol{\varepsilon}^{p})\Big]\, dV - \int_\Omega \mathbf{w} \cdot \mathbf{b}\, dV = 0 \ , \tag{18}$$

where $\boldsymbol{\varepsilon}(\mathbf{u} = \frac{1}{2}\big(\nabla \mathbf{u} + (\nabla \mathbf{u})^T\big)$. This form represents the global force equilibrium between applied external loads and interal stress states. Due to nonlinearity between stress and strain relations, it must be appropriately linearized to drive this residual to zero (equilibrium) through iterative correction using Newton's method (solving a linear system to determine the next correction to the solution). This linearization of $\mathcal{R}$ is sought at current iterate $\mathbf{u}^{(k)}$, such that $\mathbf{u}^{(k+1)} = \mathbf{u}^{(k)} + \Delta\mathbf{u}$. Thus, $\Delta\mathbf{u}$ is sought so that the residual increment vanishes to first order (Taylor approximation) for

$$\mathcal{R}(\mathbf{u}^{(k)} + \Delta\mathbf{u}) \approx \mathcal{R}(\mathbf{u}^{(k)}) + D\mathcal{R}[\Delta\mathbf{u}] = 0 \ , \tag{19}$$

where the Gateaux derivative $D\mathcal{R}[\Delta\mathbf{u}] = \int_\Omega \nabla \mathbf{w} : \delta\boldsymbol{\sigma}\, dV$. This leads to

$$D\mathcal{R}[\Delta\mathbf{u}] = \int_\Omega \nabla \mathbf{w} : \frac{\partial \boldsymbol{\sigma}}{\partial \boldsymbol{\varepsilon}} : \big(\boldsymbol{\varepsilon}(\Delta\mathbf{u}) - \delta\boldsymbol{\varepsilon}^{p} - \delta\boldsymbol{\varepsilon}^{th}\big)\ dV \ , \tag{20}$$

where the thermal strain increment $\delta\boldsymbol{\varepsilon}^{th}$ is already known and can be subtracted before hand. The plastic strain increment $\delta\boldsymbol{\varepsilon}^{p}$ is determined from the return-mapping procedure (discussed in the following section), which determines the correction to the stress state for the current $\mathbf{u}^k$. The final system to solve via Newton's method is

$$\int_\Omega \nabla \mathbf{w} : \frac{\partial \boldsymbol{\sigma}}{\partial \boldsymbol{\varepsilon}} : (\boldsymbol{\varepsilon}(\Delta\mathbf{u}))\ dV = -\mathcal{R}(\mathbf{u}^{(k)}) \ . \tag{21}$$

Due to the fact that plastic deformations are modelled as rate equations as per the flow theory, the problem must be solved using the finite thermal strain increment for every mechanical load step. The solution, is a fixed displacement increment $\Delta\mathbf{u}$ instead of the total displacement $\mathbf{u}$. Thus, the Newton method seeks a correction $\delta\mathbf{u}$ to this increment, in every iteration k, to drive the linearized residual to zero (maintaining equilibrium) while also ensuring the return mapping procedure (constitutive update) is satisfied.

3. NUMERICAL IMPLEMENTATION

An implementation of the thermal and mechanical weak forms can be carried out using the Finite Element Method.[33,34] However, FEM is only a spatial discretization technique, and therefore the thermal weak form must be also be discretized for the time domain, so that the finite temperature increments can be computed, as well as the subsequent thermal strain increments which are then coupled to the mechanical problem. For the mechanical problem, each strain increment generates an external loading state, defining the residual, and the global force equilibrium to be solved. The Newton solve is performed for this residual until convergence, to determine the displacement increment. During each iteration of this Newton solve, a consistent tangent matrix needs to be built from the bilinear part of the weak form since linearization of the weak form must also include proper linearization of the stress computation algorithm.[35] Thus, while solving the global equilibrium, a local constitutive problem must also be solved. This local problem ensure that the stress is appropriately adjusted or *projected* (in each Newton iteration) within the yield surface to ensure algorithmic consistency (should plastic deformation be present). In short, the full mechanical problem consist of simulateneously solving a global force equilibrium for the displacements, as well as local constitutive equilibrium for the strains, for every iteration of the Newton solver. The global problem is solved for the nodal degrees of freedom of the FEM mesh (due to nodal interconnectivity), while the local problem is solved for the Gauss-points (since it is a material balance and thus purely within the element).[36]

3.1 Time stepping scheme

For a temporal discretization of the thermal weak form, a time stepping scheme is necessary. Let time be discretized as $t_{n+1} = t_n + \Delta t$ (where $t_0 = 0$), with $T_n = T(\mathbf{x}, t_n)$. Here, the Crank–Nicolson scheme is used which is a semi-implicit time time stepping scheme.[37] Here n is the index of the current time step and $n+1$ is the index of the next timestep, hence

$$\frac{\partial T}{\partial t} \approx \frac{T_{n+1} - T_n}{\Delta t}, \quad T \approx \frac{T_{n+1} + T_n}{2} \ . \tag{22}$$

Thus, find $T_{n+1} \in V$ such that for all $v \in V$:

$$\begin{aligned} &\int_\Omega \rho c_p \frac{T_{n+1} - T_n}{\Delta t} v \, d\mathbf{x} + \int_\Omega k \nabla \left(\frac{T_{n+1} + T_n}{2} \right) \cdot \nabla v \, d\mathbf{x} \\ &+ \int_{\partial\Omega \setminus (\Gamma_l \cup \Gamma_b)} h \left(\frac{T_{n+1} + T_n}{2} - T_0 \right) v \, dS \\ &+ \int_{\Gamma_l} h_{rad} \left(\frac{T_{n+1} + T_n}{2} - T_0 \right) v \, dS v \, dS = \int_\Omega Q_{n+1}(\mathbf{x}) v \, d\mathbf{x} \end{aligned} \tag{23}$$

where $Q_{n+1}(\mathbf{x})$ is evaluated explicitly using the known position of the moving heat source at time t_{n+1}. The time step size Δt is chosen by taking both stable advection diffusion into consideration, via the Courant-Friedrichs-Lewy condition (CFL), as well as limiting heat source movement over a sufficiently fine resolution of the mesh in every time step.[38] Therefore, two time step sizes, Δt_Ω and Δt_L, are computed

$$\Delta t_\Omega = \mathrm{CFL} \frac{(\Delta s)^2}{\kappa}, \quad \Delta t_L = R_L \frac{\Delta l}{v_s} \ , \tag{24}$$

where CFL is set to 0.5, Δs is the smallest element size, v_s is the velocity of the laser beam and Δl is the element size in the movement direction. R_L is the relative beam shift to limit the movement step to a fraction of the element size (in this case 0.4) ensuring temperature variation is well approximated by basis functions within the element. Thus, the accepted time step Δt is

$$\Delta t = \min(\Delta t_\Omega, \Delta t_L) \ . \tag{25}$$

Thermal properties at different temperatures have been extracted from literature. Implementation was based on a conditional check of the temperature field, to update material properties in the weak form where needed,

during each time step. Some simplifications and assumptions have been made to allow for computational feasibility. The thermal model tapers off the upper temperature limit to the vaporization temperature using a basic latent heat flux model to simulate high energy losses at vaporization although these temperature were not reached during the simulation. For plastic analysis and solidification study, where surface level effects or keyhole physics are of little interest, this assumption also allows for reasonable computational speedup as the meltpool (including the vapor capillary) itself is stress free.

3.2 Linearized Residual

The plasticity calculations are computed in increments of stress and strain due to the rate form in the flow rule. Therefore, it is necessary to solve the global mechanical problem (force equilibrium) for displacement increments $\Delta\mathbf{u}$ instead of displacement. This allows for control of the loading step size for the problem and thus maintains stable convergence of the Newton solver during plastic deformation by appropriately recomputing the Gateaux derivative (or tangent stiffness) of the problem during plastic evolution. Thus, in an incremental sense, the mechanical weak form becomes

$$\mathcal{R}_{n+1}(\Delta\mathbf{u}) = \int_\Omega \nabla\mathbf{w} : \boldsymbol{\sigma}(\mathbf{u}_n + \Delta\mathbf{u})\, dV - \int_\Omega \mathbf{w}\cdot\mathbf{b}\, dV = 0 \ , \tag{26}$$

where

$$\boldsymbol{\sigma}(\mathbf{u}_n + \Delta\mathbf{u}) = \mathbb{C} : \left(\boldsymbol{\varepsilon}(\mathbf{u}_n + \Delta\mathbf{u}) - \boldsymbol{\varepsilon}^{th}(\Delta T) - \boldsymbol{\varepsilon}^{p}\right) \ , \tag{27}$$

and $\boldsymbol{\varepsilon}^{th}(\Delta T) = \alpha\Delta T\mathbf{I}$. Further simplification leads to

$$\mathcal{R}_{n+1}(\Delta\mathbf{u}) = \int_\Omega \nabla\mathbf{w} : \mathbb{C} : \left(\boldsymbol{\varepsilon}(\mathbf{u}_n + \Delta\mathbf{u}) - \boldsymbol{\varepsilon}^{th} - \boldsymbol{\varepsilon}^{p}\right)\, dV - \int_\Omega \mathbf{w}\cdot\mathbf{b}\, dV = 0 \ . \tag{28}$$

Instead of solving for the whole displacement in one load step, the solution is now sought in increments of displacement for given load increments (applied via the thermal strain increments), where the global force equilibrium must be solved for an unknown displacement increment $\Delta\mathbf{u}$. The linearization of this incremental form is now focused on determining a *correction* to the displacement increment $\delta\mathbf{u}$ such that

$$\Delta\mathbf{u}^{(k+1)} = \Delta\mathbf{u}^{(k)} + \delta\mathbf{u} \ , \tag{29}$$

and then

$$\mathcal{R}_{n+1}(\Delta\mathbf{u}^{(k)} + \delta\mathbf{u}) \approx \mathcal{R}_{n+1}(\Delta\mathbf{u}^{(k)}) + D\mathcal{R}[\delta\mathbf{u}] = 0 \ , \tag{30}$$

where the Gateaux derivative is

$$D\mathcal{R}[\delta\mathbf{u}] = \int_\Omega \nabla\mathbf{w} : \frac{\partial\boldsymbol{\sigma}}{\partial\boldsymbol{\varepsilon}} : \left(\boldsymbol{\varepsilon}(\delta\mathbf{u}) - \delta\boldsymbol{\varepsilon}^{p} - \delta\boldsymbol{\varepsilon}^{th}\right)\, dV \ . \tag{31}$$

Solving this system results in the correction to the displacement increment $\delta\mathbf{u}$, which is then used to adjust the value of the increment itself $\Delta\mathbf{u}$ according to Eq. (29), until convergence is reached ($\|\mathcal{R}\| \approx 0$). The final increment $\Delta\mathbf{u}_k$, at the end of the converged iteration k, is then used to update the total displacement $\mathbf{u}$ at the end of every load step.

3.3 Return mapping - Stress projection

Concurrent to solving the global force equilibrium, the local constitutive equilibrium must also be solved in every iterative correction. This ensures that (in case of plastic deformation) the stress is the *true* stress state $\boldsymbol{\sigma}^{n+1}$ which will be used by the global weak form. The term $\mathbb{C} : \left(\boldsymbol{\varepsilon}(\mathbf{u}_n + \Delta\mathbf{u}) - \boldsymbol{\varepsilon}^{th} - \boldsymbol{\varepsilon}^{p}\right)$ is the stress after correction. This thermal strain can be computed explicitly but for plastic strain, a return mapping procedure must be employed to determine it which will subsequently also determine the stress correction to the stress state (should stress surpass yield). This correction projects this stress state back on to the yield surface, thus maintaining the consistency condition, in every iteration, once plastic deformation has started (otherwise the correction is zero during elastic deformation). This is done via the return mapping procedure, which checks the yield condition to

determine plastic deformation quantities like the yield surface normal $\frac{\partial f}{\partial \boldsymbol{\sigma}}$, the plastic multiplier $\Delta\lambda = \Delta p$ and the stress correction.[39,40]

The plastic multiplier Δp is itself a function of the strain increment $\Delta\boldsymbol{\varepsilon}$, generated by the given displacement increment $\Delta\mathbf{u}$, which in turn is a function of stress σ but it is also this stress that depends on the plastic strain increment. Hence, in most cases, the local constitutive solve is also a nonlinear problem for the plastic strain increment. However, for this case, it can be directly computed, as an explicit closed-form solution because of the given von Mises yield criterion.[41] The starting point of the return mapping begins with computing the trial stress $\boldsymbol{\sigma}^{tr}$ which is the sum of the stress at previous load state (already projected back or previously elastic), and the stress increment generated from the current displacement increment (adjusted for the precalculated thermal strains)

$$\boldsymbol{\sigma}^{tr}_{n+1} = \boldsymbol{\sigma}_n + \mathbb{C} : (\boldsymbol{\varepsilon}(\Delta\mathbf{u}) - \boldsymbol{\varepsilon}^{th}) \ . \tag{32}$$

Defining $\boldsymbol{s}_{n+1} = \boldsymbol{\sigma}^{tr}_{n+1} - \frac{1}{3}\mathrm{tr}(\boldsymbol{\sigma}^{tr}_{n+1})\mathbf{I}$, as the deviatoric part of stress and $\sigma_{eq} = \sqrt{\frac{3}{2}(\boldsymbol{s} : \boldsymbol{s})}$, the yield function can be stated as

$$f = (\sigma_{eq})_{n+1} - \sigma_0 - Hp_n \ . \tag{33}$$

This yield function compares the previous stress state $\boldsymbol{\sigma}_n$ and the current trial state $\boldsymbol{\sigma}^{tr}_{n+1}$ to determine if yielding has occured during the current displacement increment $\Delta\mathbf{u}$. In case plastic deformation occurs on the given increment, the accumulated plastic strain δp needs to be computed. For the given von Mises yield criterion, this term can be derived from the constraint on the flow rule, due to the consistency conditions i.e., $f(\boldsymbol{\sigma}, p) = 0$ and thus

$$\delta f = \frac{\partial f}{\partial \boldsymbol{\sigma}} : \delta\boldsymbol{\sigma} + \frac{\partial f}{\partial p} : \delta p = 0 \ , \tag{34}$$

where $\frac{\partial f}{\partial p} = H$. Additionally, via the constitutive law, $\delta\boldsymbol{\sigma} = \mathbb{C} : (\delta\boldsymbol{\varepsilon} - \delta\boldsymbol{\varepsilon}^p)$. Also from the flow rule $\dot{\boldsymbol{\varepsilon}}^p = \dot{p}\frac{\partial f}{\partial \boldsymbol{\sigma}}$, the plastic strain can be written as

$$\delta\boldsymbol{\varepsilon}^p = \delta p \frac{\partial f}{\partial \boldsymbol{\sigma}} + p\delta\big(\frac{\partial f}{\partial \boldsymbol{\sigma}}\big) \ . \tag{35}$$

During return mapping algorithm, the yield surface normal $\frac{\partial f}{\partial \boldsymbol{\sigma}}$ is treated as fixed so $\delta\boldsymbol{\varepsilon}^p = \delta p\Big(\frac{\partial f}{\partial \boldsymbol{\sigma}}\Big)$. Thus, the final expression for $\delta\boldsymbol{\sigma}$ is $\delta\boldsymbol{\sigma} = \mathbb{C} : \Big(\delta\boldsymbol{\varepsilon} - \delta p\frac{\partial f}{\partial \boldsymbol{\sigma}}\Big)$ which when substituted into Eq. (34) gives

$$\begin{aligned} \delta f &= \frac{\partial f}{\partial \boldsymbol{\sigma}} : \left[\mathbb{C} : \left(\delta\boldsymbol{\varepsilon} - \delta p\frac{\partial f}{\partial \boldsymbol{\sigma}}\right)\right] + \frac{\partial f}{\partial p} : \delta p = 0 \\ \Rightarrow \delta p &= \frac{\frac{\partial f}{\partial \boldsymbol{\sigma}} : \mathbb{C} : \delta\boldsymbol{\varepsilon}}{\frac{\partial f}{\partial \boldsymbol{\sigma}} : \mathbb{C} : \frac{\partial f}{\partial \boldsymbol{\sigma}} + H} \ . \end{aligned} \tag{36}$$

With this, an expression for the plastic multiplier δp has been derived. Since this is dependent on the actual strain increment $\delta\boldsymbol{\varepsilon}$, an iterative process is needed to find a solution. However, for a von Mises yield criterion with isotropic hardening, a closed-form solution for Δp can be derived for a finite strain increment $\Delta\boldsymbol{\varepsilon}$. Given $\frac{\partial \sigma_{eq}}{\partial \boldsymbol{\sigma}_{ij}} = \frac{\partial f}{\partial \boldsymbol{\sigma}}$ ($\frac{\partial f}{\partial \boldsymbol{\sigma}}$ is the gradient of σ_{eq}), the yield criterion $f = (\sigma_{eq})_{n+1} - \sigma_0 - Hp_n$ can also be written as

$$\begin{aligned} f &= (\sigma_{eq})_{n+1} - \sigma_0 - Hp_n \\ \Rightarrow &= \frac{\partial \sigma_{eq}}{\partial \boldsymbol{\sigma}} : \boldsymbol{\sigma}^{tr}_{n+1} - \sigma_0 - Hp_n = \frac{\partial f}{\partial \boldsymbol{\sigma}} : \boldsymbol{\sigma}^{tr}_{n+1} - \sigma_0 - Hp_n \\ \Rightarrow &= \frac{\partial f}{\partial \boldsymbol{\sigma}} : [\boldsymbol{\sigma}_n + \mathbb{C} : (\boldsymbol{\varepsilon}(\Delta\mathbf{u}) - \boldsymbol{\varepsilon}^{th})] - \sigma_0 - Hp_n \ . \end{aligned} \tag{37}$$

During plastic deformation, the previous stress state is already on the yield surface (or projected back on to it), i.e. $\frac{\partial f}{\partial \boldsymbol{\sigma}} : \boldsymbol{\sigma}^{tr}_{n+1} = \sigma_0 - Hp_n$, thus

$$f = \frac{\partial f}{\partial \boldsymbol{\sigma}} : \mathbb{C} : (\boldsymbol{\varepsilon}(\Delta\mathbf{u}) - \boldsymbol{\varepsilon}^{th}) = \frac{\partial f}{\partial \boldsymbol{\sigma}} : \mathbb{C} : \Delta\varepsilon \ , \tag{38}$$

where $\varepsilon(\Delta\mathbf{u}) - \boldsymbol{\varepsilon}^{th}) = \Delta\varepsilon$ is the current strain increment. Using the constitutive relation for an isotropic material and the von Mises yield criterion, it can be shown that $\frac{\partial f}{\partial \boldsymbol{\sigma}} : \mathbb{C} : \frac{\partial f}{\partial \boldsymbol{\sigma}} = 3\mu$. Inserting this and the expression of f from Eq. (38), into the expression of δp from Eq. (36) gives

$$\Delta p = \frac{f}{3\mu + H} \ . \tag{39}$$

This is a finite incremental solution of the plastic multiplier for the given trial stress state (computed from strain increment $\Delta\boldsymbol{\varepsilon}) = \boldsymbol{\varepsilon}(\Delta\mathbf{u})$. The value of Δp is automatically set to 0 if $f < 0$ (elastic deformation). This is an exact solution to the plastic multiplier which can be used to determine the stress projection on to the yield surface in one iteration (closed-form). To determine this projection/correction, the plastic strain increment $\Delta\boldsymbol{\varepsilon}^p$ is computed

$$\Delta\boldsymbol{\varepsilon}^p = \Delta p \frac{3}{2\sigma_{eq}} \boldsymbol{s} \ . \tag{40}$$

The trial stress state $\boldsymbol{\sigma}^{tr}$ can now be corrected for the plastic strain

$$\boldsymbol{\sigma}_{n+1} = \boldsymbol{\sigma}^{tr}_{n+1} - \mathbb{C} : \Delta\boldsymbol{\varepsilon}^p = \boldsymbol{\sigma}_{n+1} = \boldsymbol{\sigma}^{tr}_{n+1} - \mathbb{C} : \left(\Delta p \frac{3}{2\sigma_{eq}} \boldsymbol{s} \right), \tag{41}$$

which leads to

$$\Rightarrow \boldsymbol{\sigma}_{n+1} = \boldsymbol{\sigma}^{tr}_{n+1} - 3\mu \left(\frac{f}{3\mu + H} \right) \frac{\partial f}{\partial \boldsymbol{\sigma}} \ , \tag{42}$$

This stress correction, along with the yield surface normal $\frac{\partial f}{\partial \boldsymbol{\sigma}} = \frac{3}{2} \frac{\boldsymbol{s}}{\sigma_{eq}}$ and plastic multiplier Δp are all automatically set to 0 should the deformation be in the elastic regime i.e., $f < 0$. In the plastic regime, the stress is projected back onto the yield surface and the values of $\frac{\partial f}{\partial \boldsymbol{\sigma}}$ and Δp are stored for computing the algorithmically consistent tangent stiffness matrix to solve the global force equilibrium for displacement increments.

3.4 Consistent tangent matrix

The stress correction is a local process happening on integration points but must also be algorithmically represented at a global level for the force equilibrium, thus ensuring consistent calculation of the displacement increment correction δu.[35] This is due to incremental nature of the variational problem and thus a stable and consistent expression for the term $\frac{\partial \boldsymbol{\sigma}}{\partial \boldsymbol{\varepsilon}}$ (in the bilinear form) is needed. It must be corrected appropriately for plastic strain (in case yielding has occured), which is why it consists of the elastic constitutive tensor $\mathbb{C}$ adjusted with an additional term $\mathbb{C}^{\text{P}}$ to adjust the stiffness during plastic deformation

$$\frac{\partial \boldsymbol{\sigma}}{\partial \boldsymbol{\varepsilon}} = \mathbb{C} - \mathbb{C}^{\text{P}} \ , \tag{43}$$

where $\mathbb{C}^{\text{P}} = 0$ when $f < 0$ and $\mathbb{C}^{\text{P}} = \mathbb{C} : \frac{\partial \boldsymbol{\varepsilon}^p}{\partial \boldsymbol{\sigma}} : \mathbb{C}$ when $f = 0$. This is why this term is also known as the *consistent tangent operator*. Using the expression for δp, the expression for $\delta\boldsymbol{\sigma}$ can be reformulated to derive the algorithmically consistent tangent operator

$$\begin{aligned} \delta\boldsymbol{\sigma} &= \mathbb{C} : \left(\delta\boldsymbol{\varepsilon} - \delta p \frac{\partial f}{\partial \boldsymbol{\sigma}} \right) = \mathbb{C} : \delta\boldsymbol{\varepsilon} - \left(\frac{\frac{\partial f}{\partial \boldsymbol{\sigma}} : \mathbb{C} : \delta\boldsymbol{\varepsilon}}{\frac{\partial f}{\partial \boldsymbol{\sigma}} : \mathbb{C} : \frac{\partial f}{\partial \boldsymbol{\sigma}} + H} \right) \mathbb{C} : \frac{\partial f}{\partial \boldsymbol{\sigma}} = \left[\mathbb{C} - \frac{(\mathbb{C} : \frac{\partial f}{\partial \boldsymbol{\sigma}}) \otimes (\frac{\partial f}{\partial \boldsymbol{\sigma}} : \mathbb{C})}{\frac{\partial f}{\partial \boldsymbol{\sigma}} : \mathbb{C} : \frac{\partial f}{\partial \boldsymbol{\sigma}} + H} \right] : \delta\boldsymbol{\varepsilon} \\ \Rightarrow \frac{\delta\boldsymbol{\sigma}}{\delta\boldsymbol{\varepsilon}} &= \mathbb{C} - \frac{(\mathbb{C} : \frac{\partial f}{\partial \boldsymbol{\sigma}}) \otimes (\frac{\partial f}{\partial \boldsymbol{\sigma}} : \mathbb{C})}{\left(\frac{\partial f}{\partial \boldsymbol{\sigma}} : \mathbb{C} : \frac{\partial f}{\partial \boldsymbol{\sigma}} \right) + H} \ , \end{aligned} \tag{44}$$

where the term being subtracted from $\mathbb{C}$ vanishes in case of elastic deformation, but adjusts the stiffness in case of plastic deformation. Normally calculating this operator for the Newton solver is not possible in closed form and relies on automatic diffrentiation. However, considering the given yield criterion, an analytical expression

can be derived for an isotropic material, i.e., $\mathbb{C} : (\boldsymbol{\varepsilon} - \boldsymbol{\varepsilon}^p) = \lambda \operatorname{tr}(\boldsymbol{\varepsilon} - \boldsymbol{\varepsilon}^p) + 2\mu(\boldsymbol{\varepsilon} - \boldsymbol{\varepsilon}^p)$. This leads to the following expression for the consistent tangent operator

$$\frac{\delta \boldsymbol{\sigma}}{\delta \boldsymbol{\varepsilon}} = \mathbb{C} - 3\mu \left(\frac{3\mu}{3\mu + H} - \frac{3\mu(\Delta p)}{\sigma_{eq}} \right) \frac{\partial f}{\partial \boldsymbol{\sigma}} \otimes \frac{\partial f}{\partial \boldsymbol{\sigma}} - 2\mu \frac{3\mu(\Delta p)}{\sigma_{eq}} \mathbb{DEV} \ , \tag{45}$$

where $\mathbb{DEV}$ is the deviatoric operator on a fourth order tensor. Here, the plastic multiplier Δp and the yield surface normal $\frac{\partial f}{\partial \boldsymbol{\sigma}}$, computed from the stress projection step, are used for evaluating this operator. Upon discretizing this in the weak form via the FEM, this operator is then appropriately called *tangent stiffness matrix*. In a more general sense, it is the ratio of the infinitesmal change in stress for an infinitesmal change in strain.

With the stress projection, plastic increment and tangent stiffness matrix determined, the weak form of the linearized residual can be solved to compute the correction to the displacement increment $\delta \mathbf{u}^{(k)}$ which adjusts the displacement increment $\Delta \mathbf{u}_n$ in every iteration. The convergence criteria here is to drive the norm of the linearized residual to a small enough value i.e, $\|\mathbf{R}^{(k)}\| < \text{tol}_{\text{NR}}$ (establish force equilibrium). The final projected stress $\boldsymbol{\sigma}_{\text{proj}}$ is then lying on the yield surface and can be stored as the stress $\boldsymbol{\sigma_{n+1}} = \boldsymbol{\sigma}_{\text{proj}}$ and the currently calculated plastic multiplier Δp will be added to the total accumulated plastic strain $p_{n+1} = p_n + \Delta p$, for the next load step. At the next load step, the current displacement increment (adjusted for corrections via iterations) $\Delta \mathbf{u}_{n+1} = \Delta \mathbf{u}_n^{(k)}$ is then used for determining the strain for the trial stress, and so the sequence is repeated for all load steps. The complete algorithm for the entire elastoplastic calculation is shown in Appendix A.

Essentially, the algorithm solves the local problem and global problem simulateneously in every iteration of the Newton-Raphson scheme such that local changes are reflected in the global problem and vice versa. Thus, both local variables such as stress and plastic strain, as well as global displacements, are updated every iteration. The implementation of the complete algorithm is carried out in the open source library for solving PDEs: FENICs.[36] Its interface in Python, DOLFINx, is used to implement the entire framework of the problem in a variational form for the FEM.[42] The Python interface, which allows for more intuitive implementation of weak forms using the Unified Form Language, is balanced by the computational speed up provided by the C++ code compiled in real time.[43] Another advantage is that it allows more freedom in the use of a variety of preconditioners and solvers as well as parallel programming capabilities.[44–46]

3.5 Proposed Approach for Mechanical Problem

An additional aspect of this work is the investigation of a more efficient approach for the mechanical model, particularly the acceleration of solving the global problem during the plasticity load steps. It is well established that the mechanical problem (especially if it is nonlinear) can take upto 10 times longer to solve per step compared to a thermal problem iteration.[47] Primarily, this stems from the fact that a displacement vector has 3 components, and thus 3 degrees of freedom (DOFs), per mesh vertex, compared to temperature which is a scalar[48] and has only one DOF per vertex. Moreover, for a nonlinear problem the material update can also involve solving a nonlinear system locally (at every integration point) to enforce plasticity.[49,50] Also, a nonlinear problem requires multiple solves/iterations of the linearized residual system for one step. Additionally, the stiffness matrix for such nonlinear problems is not always symmetric and requires more expensive assembly operations.[51,52] Thus, it is worth investigating computational approaches to accelerate displacement and accompanying stress/plastic strain calculations for computational efficiency. This study aims to investigate a novel way to solve the nonlinear mechanical weak form such that the plasticity calculations can be accelerated.

Explicit integration schemes for incremental stepping approaches are used for time integration of dynamic problems.[51] Since plastic evolution in rate-independent plasticity is analogous to *pseudo-time stepping*, explicit integration schemes can also be used for local material updates. Such techniques strive to reduce computational effort of the global force equilibrium problem as well. One such way is to investigate a purely *explicit* approach to the global problem as well, provided the plastic variables and stress projection in plastic deformation can be analytically computed beforehand. These approaches have showcased that as the degrees of freedom (DOF) grow, such explicit approaches can outperform classical implicit approaches.[49] Thus, in to save the computational effort of computing the nonlinear terms of the consistent tangent stiffness (those that correspond to plastic

deformation), the proposed approach in this study, moves these nonlinear terms onto the right side of the weak form as part of the residual as a *quasi* additional internal force. This is essentially, a fixed point linearization of the problem about the current plastic deformation state, treating its contribution to the weak form explicitly rather than implicitly as is normally done in case of a Newton solve. This approach will henceforth be stated as a *Quasi-Newton* scheme when compared with the traditional *True-Newton* scheme for the purposes of this study.

To showcase the modified Quasi-Newton approach, the linearized form of the residual derived previously (ignoring any body forces) is stated

$$\int_\Omega \nabla \mathbf{w} : \frac{\partial \boldsymbol{\sigma}}{\partial \boldsymbol{\varepsilon}} : \boldsymbol{\varepsilon}(\delta \mathbf{u})\, dV = -\int_\Omega \boldsymbol{\sigma}_{\text{proj}} \left(\boldsymbol{\varepsilon}(\Delta \mathbf{u}) - \boldsymbol{\varepsilon}^p - \boldsymbol{\varepsilon}^{th}\right) : \nabla \mathbf{w}\, dV \ . \tag{46}$$

With $\mathbf{w} = \delta \mathbf{u}_{\mathbf{test}}$ and knowing that $\frac{\partial \boldsymbol{\sigma}}{\partial \boldsymbol{\varepsilon}} = \mathbb{C} - \mathbb{C}^{\text{p}}$, for a Newton iterate k it can be written

$$\int_\Omega \boldsymbol{\varepsilon}(\delta \mathbf{u}_{\mathbf{test}}) : (\mathbb{C} - \mathbb{C}^{\text{p}}) : \boldsymbol{\varepsilon}(\delta \mathbf{u}^{(k)})\, dV = -\mathcal{R}^{(k)}(\boldsymbol{\varepsilon}(\Delta \mathbf{u})) : [(\delta \mathbf{u}_{\mathbf{test}})] \ , \tag{47}$$

i.e., in matrix form

$$(\mathbf{K} - \mathbf{K}^{\text{p}})\, \delta \mathbf{U}^{(k)} = -\mathbf{R}^{(k)} \ . \tag{48}$$

This is the typical iteration for a True-Newton (Newton-Raphson) which usually yields *quadratic convergence* locally.[53] However, this requires the computation and inversion of the stiffness $\mathbf{K} - \mathbf{K}^{\text{p}}$ at every iteration k. As mentioned earlier, it consists of an elastic stiffness $\mathbf{K}$ and plastic correction $\mathbf{K}^{\text{p}}$. For the Quasi-Newton approach, only the elastic part of the tangent stiffness is kept on the left and plastic correction is treated explicitly (by moving towards the right)

$$\mathbf{K}\, \delta \mathbf{U}^{(k)} = -\mathbf{R}^{(k)} + \mathbf{K}^{\text{p}}\, \delta \mathbf{U}^{(k-1)} \ , \tag{49}$$

which then updates

$$\Delta \mathbf{U}^{(k)} = \Delta \mathbf{U}^{(k-1)} + \delta \mathbf{U}^{(k)} \ , \tag{50}$$

until convergence is reached. This is now a fixed point linearization of the already linearized weak form which solves the problem around the *current* plastic state (Picard iteration).[48,54,55] The advantage here being that the stiffness, having only elastic contribution, must only be computed and inverted once in the beginning of the load step

$$\mathbf{K}^{(0)}\, \delta \mathbf{U}^{(k)} = -\mathbf{R}^{(k)} + \mathbf{K}^{p}\, \delta \mathbf{U}^{(k-1)} \ . \tag{51}$$

The disadvantage of this approach is the loss of the convergence rate since we do not solve for the true linearized tangent stiffness (it is not algorithmically consistent anymore) at every iteration which introduces additional truncation errors that lead to less accurate solutions, by causing overshoots or undershoots, unless the residual is driven to lower tolerance or smaller load steps. This stems from the fact that the plastic state essentially *lags* behind the true state by one iteration solve. Additionally, the inclusion of the plastic terms in the residual introduces a *modified* global force equilibrium, as the plastic terms are being essentially applied as extra *quasi* forces. This leads to more iterations needed to reach convergence for a specific load step, especially when plastic deformation is large. However, in large degree of freedom systems, the benefit of the single time factorization of the stiffness (and the simple back solve) can be magnitudes of order cheaper than refactorization every time which usually outweighs the cost of additional iterations.[56] One way to stabilize the stiffness matrix (for Quasi-Newton) overshoots and undershoots, as we near the *root* is by dampening the explicit (nonlinear) parts of the residual which can help to prevent oscillations of the residual norm near the root

$$\mathbf{K}_0\, \delta \mathbf{U}^{(k)} = -\mathbf{R}^{(k)} + \omega \mathbf{K}^{p}\, \delta \mathbf{U}^{(k-1)} \ , \tag{52}$$

where ω is the damp factor and is $0 \leq \omega \leq 1$. This approach, admittedly, leads to slower convergence because the steps taken to get to the root are smaller, and thus it takes longer converge. Nevertheless, fine-tuning the damping factor results in reaching a stable solution, during plastic deformation, even with a constant stiffness by minimizing these spurious oscillations.

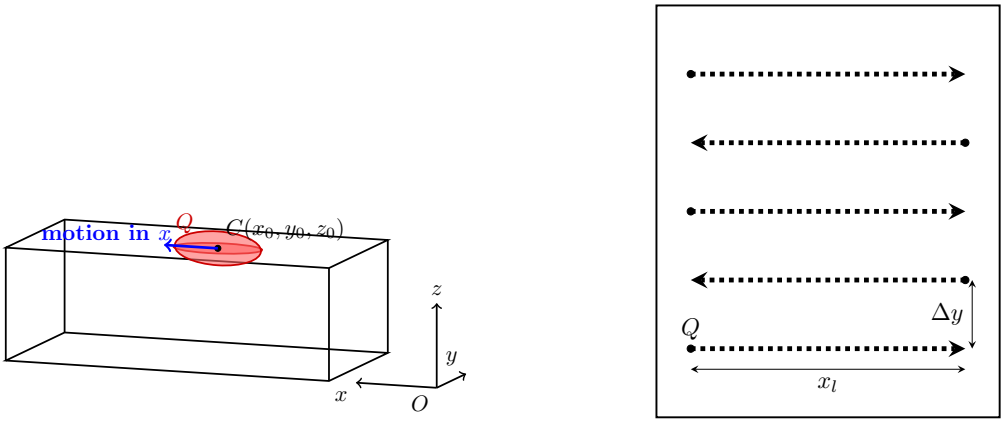

(a) (b)

Figure 1: (a) 3D representation of thermomechanical benchmark problem. The heat source Q moves in the $+x$ direction at the beginning starting at center $C = (x_0, y_0, z_0)$ (b) A typical scan strategy for a moving laser beam with track length x_l and track spacing Δy.

4. PROBLEM DEFINITION

The main goal of this research is to showcase track level simulation of the LPBF process, to illustrate the efficacy and validity of the proposed thermomechanical model. Therefore, an appropriate thermomechanical benchmark problem will be defined to ensure the model produces physically feasible and valid results that can eventually be studied and analyzed. However, further variation and flexibility in the model parameters will also be implemented for validating with other similar models. To investigate and highlight computational efficiency of the Quasi-Newton approach, a seperate mechanical benchmark is also studied which will be used to analyze and illustrate potential benefits of the Quasi-Newton approach as the size of DOFs increases.

4.1 Thermomechanical benchmark problem

The governing equations, weak form and boundary conditions defined in Sec. 2 are used to study a rectangular domain on which the laser beam will be incident. The heat source modelling will therefore be on the top surface as well as the radiation boundary condition will be on the top surface Γ_l. As shown in Fig. 1a, the heat source Q begins its movement on top of the top domain in the $+x$ direction. After moving a certain track length x_l, the heat source jumps in the $+y$ direction by a certain track spacing Δy before rotating 180 degrees and moving backwards in the $-x$ direction and so onwards, as shown in Fig. 1b. The domain size is set to $\Omega = \{(x, y, z) \mid 0 \leq x \leq 2.2, -0.8 \leq y \leq 1, 0 \leq z \leq 0.5\}$ in mm. $x_l = 1$ mm and $\Delta y = 0.05$mm, with the following track sequence

Track 1 – Start: $(0.44, 0.1)$	End: $(1.44, 0.1)$,
Track 2 – Start: $(1.44, 0.15)$	End: $(0.44, 0.15)$,
Track 3 – Start: $(0.44, 0.2)$	End: $(1.44, 0.2)$,
Track 4 – Start: $(1.44, 0.25)$	End: $(0.44, 0.25)$,
Track 5 – Start: $(0.44, 0.3)$	End: $(1.44, 0.3)$,

where the movement is on the very top surface (incidence of laser beam) $z = 0.5$mm. The track spacing has been selected to ensure sufficient overlap and thus sufficient melting of powder but also to limit overheating and excessive melting of the powder.[15] A practical choice for the heat source, as mentioned in Sec. 2, is the Goldak heat source, illustrated in Fig. 2. The Goldak heat source accurately models the depth of heat deposition into the material for high power intensity sources such as the laser. Furthermore, it estimates the peak temperatures inside the meltpool and thus approximates the meltpool shape better.[27] It has the following analytical expression

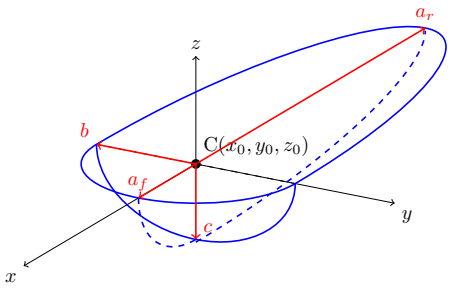

Figure 2: A schematic of the 3D double ellipsoidal heat source model proposed by Goldak *et al.* with center C and dimensions: front radius (a_f), rear radius (a_r), half width (b) and depth (c).

$$q(x,y,z,t) = \begin{cases} q_f(x,y,z,t) = \dfrac{6\sqrt{3}\,\eta P, f_f}{\pi\, a_f\, b\, c} \exp\Big[-3\left(\frac{[x-v\,t]^2}{a_f^2} + \frac{y^2}{b^2} + \frac{z^2}{c^2}\right)\Big], & x - v\,t \geq 0, \\ q_r(x,y,z,t) = \dfrac{6\sqrt{3}\,\eta P, f_r}{\pi\, a_r\, b\, c} \exp\Big[-3\left(\frac{[x-v\,t]^2}{a_r^2} + \frac{y^2}{b^2} + \frac{z^2}{c^2}\right)\Big], & x - v\,t < 0. \end{cases} \tag{53}$$

where P is laser power, v is scan speed along x, and η is absorptivity. The relative distribution of the heat source is governed by the distribution f_f and f_r where

$$f_f = \frac{2}{1 + \dfrac{a_f}{a_r}}\,, \quad f_r = \frac{2}{1 + \dfrac{a_r}{a_f}}\,. \tag{54}$$

The two terms f_f and f_r represent the relative fractions of heat deposited to the front part and the rear part of the heat source respectively. They are defined such that $f_r + f_f = 2$. Normally, the front radius a_f and halfwidth b are set to the beam radius r_b while the rear radius a_r and depth c are calibrated from process parameters to properly simulate both laser beam and generated meltpool. Since calibration is not the focus of this study, the dimensions have been adopted from previously published calibration studies.[57] The constant parameters for the thermomechanical benchmark are listed in Table 1. Thermal conductivity k, specific heat capacity c_p, material density ρ and yield stress σ_y are treated as temperature dependent. For the sake of computational efficiency, the property value is based on temperature ranges as stated in Table 2. These material and process parameters were adopted from a more complex capillary-based and potential flow meltpool model which studies meltpool dynamics during LPBF of IN 718, and was published by the authors' project partner.[58] The temperature dependence was approximated from their results and also supplemented from other literature.[59]The approximate radiation coefficient h_{rad} is linearized around a temperature difference $T_n - T_0$ according to:[60]

$$h_{rad} = \epsilon\sigma\ (T_n + T_0)\ (T_n^2 + T_0^2)\ . \tag{55}$$

The temperature T_n here is the current, solved for, temperature at a given timestep. Since powder and liquid phase have negligible stiffness, and thus negligible influence on stress and mechanical deformation, the Young's Modulus E and thermal expansion coefficient α are set to extremely small values (1% of dense material) for these phases in the mechanical simulation.

Computational efficiency for the full thermomechanical model is evaluated using central processing unit (CPU) times for different DOFs to see how the performance improves with multiple processors. To maintain reasonably accuracy with computational effort, the mechanical problem is solved after every few number of thermal steps.

Table 1: Material and process parameters - Thermomechanical benchmark.

Quantity	**Value (unit)**
Track length (x_l)	1 mm
Track spacing (Δy)	0.05 mm
Laser beam radius (r_b)	80 μm
Laser power (P)	285 W
Scan speed (v)	960 $\frac{\text{mm}}{\text{s}}$
Absorption coefficient (η)	0.7
Melting temperature (T_{melt})	1620 K
Ambient temperature (T_0)	294 K
Convection heat transfer coefficient (h)	1×10^{-4} $\frac{\text{W}}{\text{mm}^2\ \text{K}}$
Thermal expansion coefficient (α)	1.3×10^{-5} K^{-1}
Young's Modulus (E)	200 GPa
Poisson ratio (ν)	0.3
Initial yield stress (σ_y)	1100 MPa

Because direct experimental measurements were not available for this track level model, validation relied on inter-model comparison with other relevant simulation models, that have previously been validated against experiments. Those models conducted verification either through implementing upscaling approaches to make simulations feasible or by running them for much longer time periods to fully model all track level phenomena on the large scale. While this provides useful evidence of model capability within the explored parameter space, it cannot entirely substitute for direct experimental validation of the specific geometry and material combination.

4.2 Mechanical benchmark problem

The Quasi-Newton approach higlighted in Sec. 3 is compared with a traditional True-Newton scheme using a benchmark problem. The benchmark mechanical problem is that of a hollow cylinder under internal pressure.[61] The 2D problem is solved under the plane strain assumption, thus even though x and y components are pertinent to the analysis, the problem will store stress, strain and other relevant quantities as full 3D tensors for the weak form but then the integrals are evaluated on the 2D function space defined for the displacements. For stress correction during the Newton iterations, the tensor components such as projected stress and the yield surface normal are stored in Voigt notiations as 4-component vectors (2 in-plane normal components, 1 in-plane shear

Table 2: Temperature-dependent material properties.

Phase	**Temp. range** (K)	$\boldsymbol{\rho}\left(\frac{\text{kg}}{\text{mm}^3}\right)$	$\boldsymbol{k}\left(\frac{\text{W}}{\text{mm K}}\right)$	$\boldsymbol{c_p}\left(\frac{\text{J}}{\text{kg K}}\right)$	$\boldsymbol{\sigma_y}\left(\text{MPa}\right)$
Solid	$T_0 \leq T < 600$	8.2×10^{-6}	22×10^{-3}	500	1100
	$600 \leq T < 1400$	8.1×10^{-6}	26×10^{-3}	560	500
	$1400 \leq T < T_{melt}$	7.9×10^{-6}	29×10^{-3}	620	100
Liquid	$T > T_{melt}$	7.4×10^{-6}	35×10^{-3}	750	—
Powder	$T = T_0$	3.0×10^{-6}	5×10^{-3}	440	—

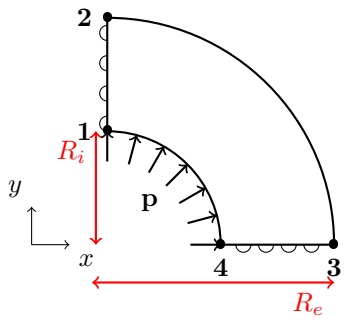

Figure 3: Quarter of the mechanical benchmark shown due to symmetric boundary conditions with inner R_i and outer R_e radii

component and 1 out-of-plane component) to take advantage of symmetry and thus simplifying linear algebra operations (not to mention it is good for memory management). They are appropriately projected to their full 3D tensor space during implementation in the weak form. For simplicity, the symmetrical nature of the problem allows for solving only one quarter of the cylinder's domain, with appropriate boundary conditions on the top left edge and bottom right edge of the quarter-cylinder, as shwon in Fig. 3. The uniform internal pressure $\mathbf{p}$ is gradually increased in load steps from 0 to just larger than the following

$$\|\mathbf{p}\| = \frac{2}{3}\sigma_0 \log\left[\frac{R_e}{R_i}\right] , \tag{56}$$

which is the analytical collapse pressure for a perfectly-plastic material.[62] The loading is applied with nonlinear spacing with smaller increments as the loading approaches yield limit. The remaining geometrical and material properties for this problem are mentioned in Table 3.

Table 3: Material and geometrical properties - Mechanical benchmark.

Quantity	**Value (unit)**
External radius (R_e)	1300 mm
Internal radius (R_i)	1100 mm
Young's Modulus (E)	70,000 MPa
Poisson's ratio (ν)	0.3
Initial yield stress (σ_0)	250 MPa

The isotropic hardening parameter H is determined by first calculating a *softer* tangent modulus E_t to model reduced stiffness during plastic deformation in the case of isotropic hardening.[29] The hardening parameter is then:

$$H = \frac{E_t\, E}{E - E_t} , \tag{57}$$

where $E_t = E/100$ for this case. Computational efficiency is evaluated using CPU times for different DOFs. The mechanical problem provides key insight into the efficiency and accuracy between both the True-Newton and Quasi-Newton approaches due to the smaller scale of the problem, thus allowing for greater flexibility for parametric studies. Error analysis for global norms as well as local point wise evaluation is conducted for comparison.

5. RESULTS AND DISCUSSION

Since the main focus of the research is the full thermomechanical model, its effectiveness and performance is studied in more detail. For that purpose, the thermomechanical model as mentioned in Sec. 3 will still use the classical True-Newton approach for solving the mechanical part and showcasing mechanical computation results. However, it is much harder to validate the mechanical part since there are very few track level models out there that show single track results for quantities such as displacements or stress. This is to be expected since the mechanical computational takes a much longer time, as illustrated, in Sec. 5.1.4 and thus the temperature history is allowed to evolve for long enough time periods over a larger scale in order to make the mechanical mesh both sufficiently accurate yet feasibly coarse for noticeable mechanical effects. Nevertheless, it is key to track the track level mechanical information as well, since, as the results will show, stress levels start to rise near track ends and in non-overlapping passes of the laser beams such that plastic strain deformation can take place in those regions due to the rapid heating and cooling cycles. This stems from the fact that the yield stress limit is reduced in regions of large temperatures, and thus requires knowledge of track-level mechanical information to keep track of local changes in stresses and plastic strains. This, then has an effect on the accuracy of larger hatch/patch level, layer level and full part level simulations.[21,47] As mentioned, an additional investigation focuses on acceleration of the computation of the mechanical problem such that the problem time can be reduced for larger and larger DOFs. To showcase that, it is reasonable to analyze the mechanical benchmark (which allows for rapid computational parameter variations) from Sec. 3 and highlight the overall solution accuracy and time for both the classical True-Newton and the proposed Quasi-Newton approach, thus highlighting any potential benefits of the Quasi-Newton approach.

5.1 Thermomechanical model

The full thermomechanical benchmark problem is a time-dependent problem and thus meaningful output data is showcased for both overall static simulation-end snapshots as well as individual track data. To further study temporal variance, plots of key quantities have also been generated and analyzed for various coordinates. Additionally, due to the lack of raw experimental data, model validations has been conducted with similar models in literature (that have been experimentally validated) and an in-depth computational performance analysis is also showcased.

5.1.1 Full simulation

At the end of the full 5-track simulation, snapshots of temperature, phase change, Z-component of displacement and Von Mises stress have been plotted in Fig. 4. Furthermore, temporal variation over time is plotted in Fig. 5 to showcase the evolution of stress with respect to temperature illustrating the effects of melting and remelting on stress development. A point based temperature plot for various probe locations is highlighted in Fig. 6 and showcases the temperature variation over time for these locations. The markers • in the plots do not individually correspond to each timestep since there are too many timesteps and that would oversaturate the plot, thus markers are added after every 10 timesteps to allow for better visualization of each plot.

Temperature variation shows that as the as the later tracks are deposited, the previous tracks start to cool down and corresponding phase change shows how full solidification starts to occur. For the more recent tracks, many areas are still molten although a smooth distinction between liquid and solid is limited by mesh resolution and visualization. Regions which cool down sooner lie at track ends and shrinked downwards due to the nearby powder, while the relatively hot newly solidifed regions have expanded upwards. Figure 5 showcases a track-by-track comparison between temperature and stress which further illustrates the stress concentration regions as they develop. It can be seen that maximum stress accumulation occurs in those same faster cooled regions where solid has not been remelted after solidification. This is likely because of the constraints by surrounding powder material and thus expansion and contraction generates the areas of stress concentration. However, further tracks need to be deposited for the yield limit in these high regions to be crossed. For the probe plots highlighted in Fig. 6, the heating and cooling cycles are evident as the heat source makes successive passes. For points P1 and P2, the cyclic effect is most dominant since the scan strategy causes significant reheating in the successive passes close to these points but points P5 and P6 do not see the cyclic variation since they are heated near the end of the simulation (lie on the last track).

The track level model showcases how regions of non-overlapping scan paths lead to the accumulation of stress which can eventually reach the yield limit and generate trapped plastic strains (due to the reduction in yield stress at high temperatures). Rapid heating and cooling cycles, especially after 30 to 40 tracks have been deposited, can lead to different regions where such plastic strains lead to embedded residual stresses. In this study, the plastic limit is not yet reached since the results have only been showcased for the first 5 tracks, and the max stress reached is apprxoimate 75 MPa. However, as showcased in Table 2, this is already close to the yield limit which has dropped in regions of high temperatures to around 100 MPa. Thus, if more tracks are studied, they will be at much higher temperatures when cooling down and lead to eventual plastic yielding. One further investigation could be to now implement a modular approach to this model for studying multiple parametric variations of larger track lengths and numbers along with a variety of scan strategies (to measure the effect of overlap). Likewise, the cooling down period after all 5 tracks was not investigated in this study. Given sufficient time, the cooldown would allow remaining molten regions to reach solid state and would cause further stress buildup as this solid state will be at very high temperatures.[21]

Linear approximation of higher order terms does approximate poorly in regions of higher temperature gradients but the boundaries being sufficiently far away from the heat source means the temperature difference will not be significant enough to pollute the boundary term with noticeable errors. Moreover, the radiation and convective terms allow for approximation of necessary heat loss at the boundaries. Nevertheless, its worth considering solving the thermal problem as a nonlinear problem with the radiation boundary term but it can lead to additional computational overhead. It must also be noted, that this model is more suited to process parameters (v_l, P, r_b) which generate a conduction-based meltpool. Thus, keyhole generation due to deep laser penetration is not studied and rather, a very simple approximation for vapor based absorption reduction is implemented. While modelling such detailed physics is not the focus of this study, due to computational feasibility, it can nevertheless be meaningful to approximate the capillary formation through other level-set techniques, such that the simulation model can be made more robust for a broader parameter set.[63]

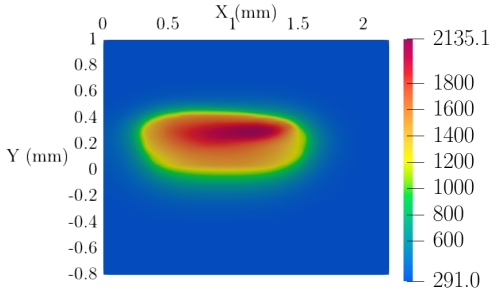

(a) Temperature (K)

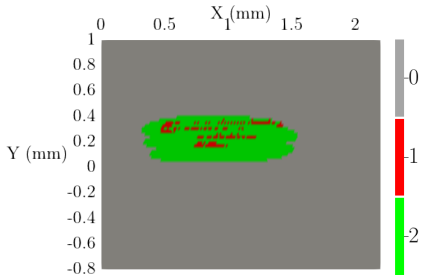

(b) Phase - 0: Powder, 1: Liquid, 2: Solid

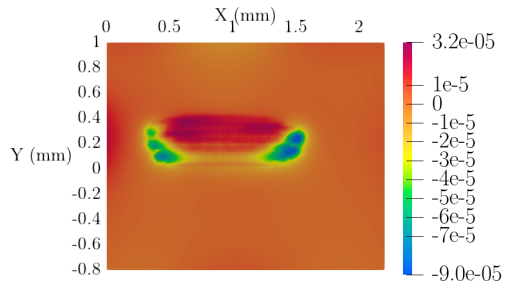

(c) Z-Component of displacement (mm)

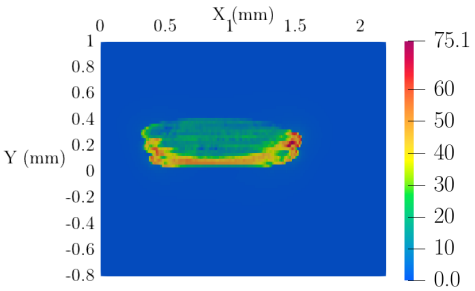

(d) Von Mises stress σ_{vm} (MPa)

Figure 4: The resulting distributions of the thermomechanical benchmark: (a) Temperature, (b) Phase change, (c) Z-component of displacement and (d) Von Mises stress, for the material properties from Table 1. The top view is shown of the surface on which laser beam is incident.

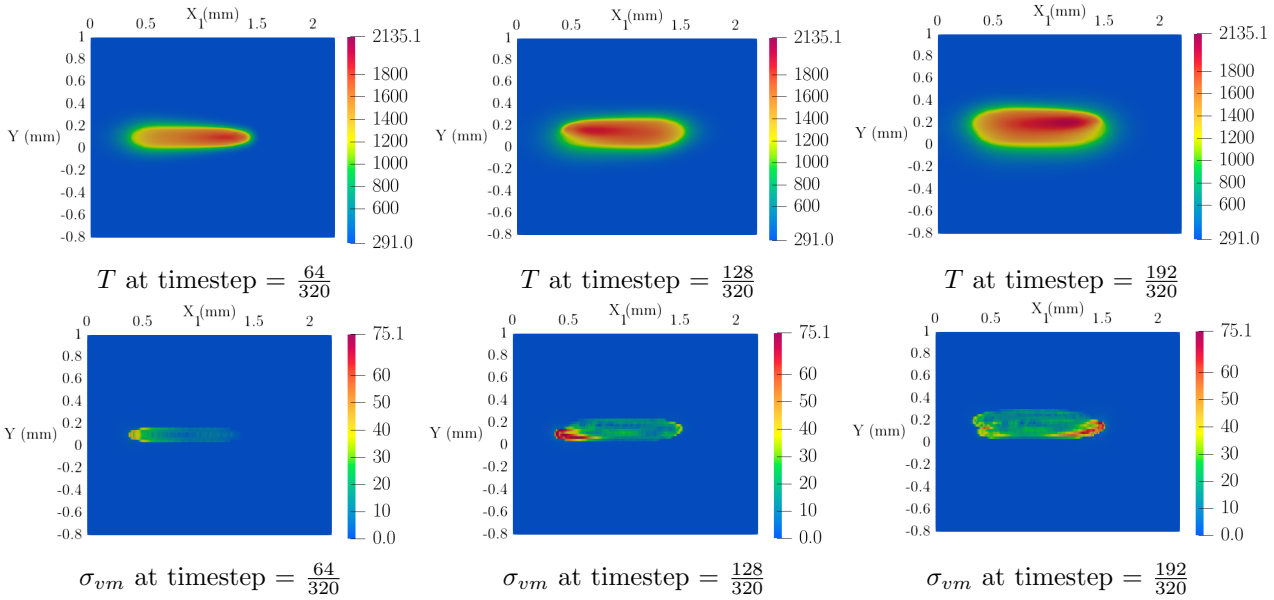

Figure 5: Temporal evolution of temperature (top row) and Von Mises stress (bottom row) at the end of the 1st track (left), 2nd track (middle) and 3rd track (right) respectively.

5.1.2 Single track

Single track variations of key quantities are also presented to study temporal variation at specific locations for steady state motion. The temperature evolution at the end of the single track is shown in Fig. 7 to better visualize what the steady state meltpool looks like from the modelled heat source. In similar fashion, the various components of displacement are also studied for the temporal evolution during first track with the X and Y components plotted on the top surface ($z = 0$). The X and Y displacement plots are shown in Fig. 8. Figure 7 illustrates how the heat source size influences the meltpool size. The black solid line represents the spatial extent of the heat source extracted from the heat source calibration studies. The front radius a_f and width $2b$ of this source are set fixed to beam radius r_b. The white solid line represents the spatial extent of the meltpool which is defined as the location of the isosurface where melting temperature is reached, $T_{iso} = T_{melt}$. Calibrated heat sources aid in developing robust simulation models but they must be recalibrated for different parameters sets. For the parameters and properties in Table 1, the heat source parameters are $a_r = c = 2r_b$. As shown and is the case for most heat source models, the actual meltpool is usually considerably longer than the heat source

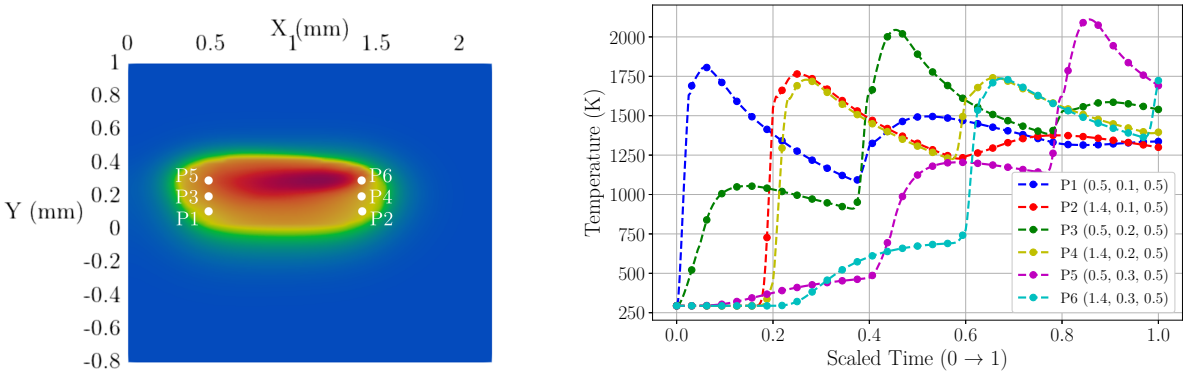

(a) (b)

Figure 6: (a) Probe locations and (b) corresponding temperature plots over time.

and the front extent of the meltpool is also longer to accurately simulate the deeper penetration of the moving laser beam.[57]

The displacement evolution clearly highlights the fact, that as temperature starts to rise, thermal expansion causes positive displacements in the x and y direction. Two situations need to be considered here, namely near the beginning of the track (left most snapshots in Fig. 8) and the end of the track (right most snapshots in

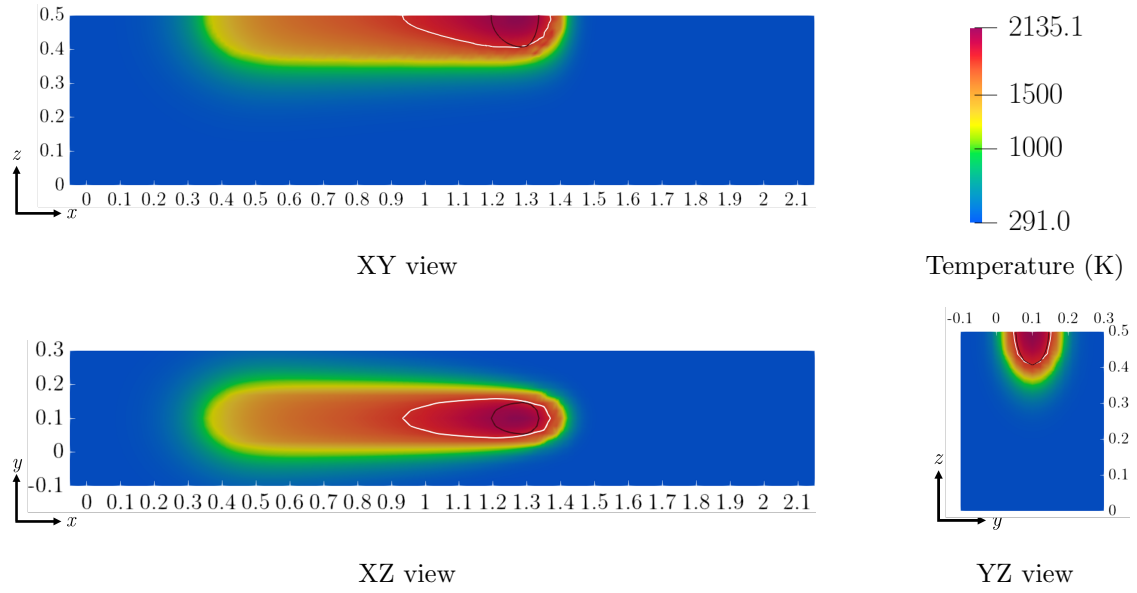

Figure 7: Orthographic views of the temperature distribution for the first track. The implemented heat source shape is marked by the black line while the resulting meltpool shape is denoted by the white line.

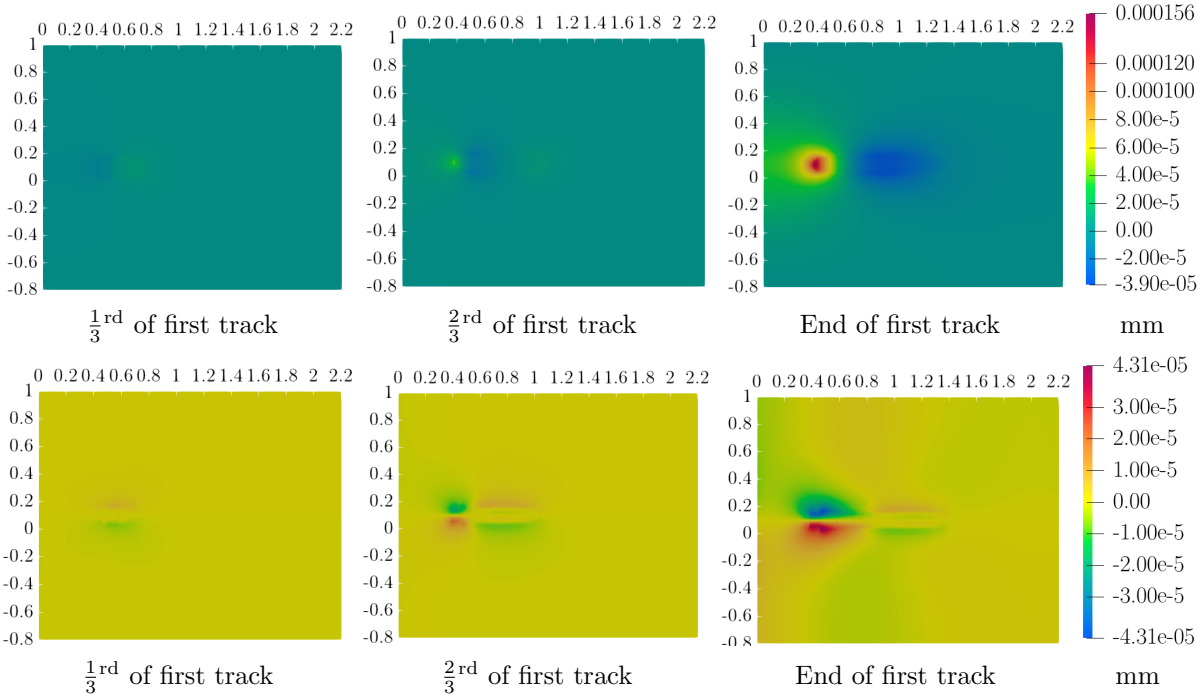

Figure 8: X-displacement (top row) and Y-displacement (bottom row) on the top surface of the domain during the evolution of the first track (x coordinates on top and y coordinates on left of snapshots).

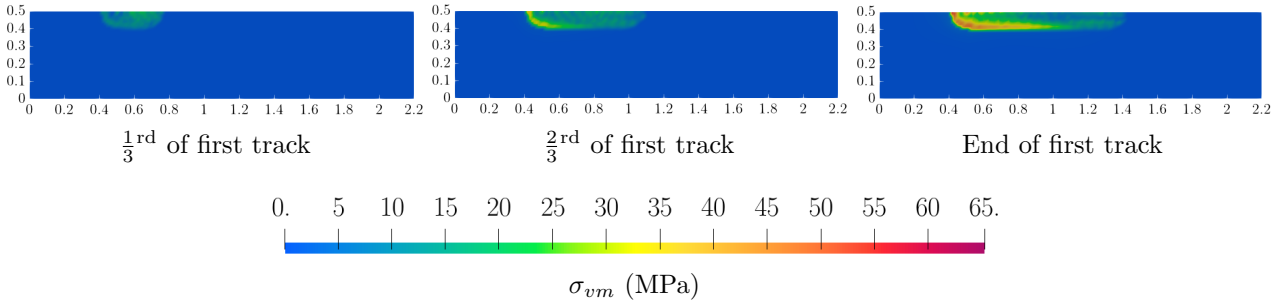

Figure 9: Von Mises stress, on the XZ cross-section of plane Y= 0.1 during the evolution of the first track (x coordinates on bottom and z coordinates on left of snapshots).

Fig. 8). In the beginning of the track, the starting track region is still molten and thus shrinkage occurs on its $+x$ side. This shrinkage leads to negative x displacements and the material upstream counters this with $+x$ displacements. Likewise this shrinkage leads to y displacements in opposing directions around the track line $y = 0.1$ with positive displacements in the area close to $y > 0.1$ and negative displacements in the area close to $y < 0.1$. Since the material is still powder, the displacements are considered small and almost negligible. At the end of the track deposition process, however, the molten region has now solidified but is still at high temperatures and thus expands in the $+x$ direction (this time with noticeable displacement) and the newly molten region upstream counters this through shrinkage. The y displacements then invert themselves appropriately to maintain equilibrium as the previously molten region is now a *hot* solid region (larger displacements) and a newly molten region exists upstream of it (smaller displacements). For stress variation, depth based evolution along the first track is showcased for the cross-section of the domain at the plane Y= 0.1. The snapshots are presented for the track evolution in Fig. 9. The variation shows what is observed in the complete simulation, but clearly highlights how initial powder and newly molten regions have no stiffness and thus no stress but upon solidification of the molten regions (near the start of the track), the stress rises sharply where the track began, as there it is mostly constrained by powder material.

5.1.3 Model validation

The complete model is compared with relevant models in literature using parameters of already published models. Since experimental results for direct comparisons are not always easily available, parameters and material models have been adapted from other models in literature, where experimental validation is conducted usually by comparing meltpool geometry. It must be noted, exact quantitative comparisons of thermal or mechanical quantities are not easily possible due to differences in model assumptions or lack of raw data, as other studies usually only publish visual representations of their simulations e.g., snapshots or plots. Additionally, at the track scale it was hard to locate studies publishing mechanical results of the models (most models studied mechanical deformation at the scale of the part or a few layer to give enough cooldown and relaxation time) but the authors were able to conduct *qualitative* stress comparisons along a single track from one other model in literature. For thermal comparison, the meltpool (and the region in its immediate vicinity) contains the largest temperature gradients and thus, temperature distributions are compared for meltpool regions to showcase how well this papers' model recreates the meltpool isosurface (since temperature variation will determine the location of this isosurface).

As mentioned in Sec. 4.1, the authors' project partners have conducted their own simulations which were more focused on a highly detailed process model calibrated from experiments for IN 718,[58] and was implemented using an open-source solver FreeFEM written using the FORTRAN language.[64] This model was computationally more challenging and restricted to the meltpool modelling itself rather than full track evolution (due to extermely large computational times) but considered the meltpool physics such as forces and effects within the meltpool as well as the formation of the vapor capillary and thus was more detailed in terms of meltpool formation and evolution from laser beam matter interaction. That is why their temperature distribution contains very large temperature values for the capillary. These were added from a seperate model because the capillary contains vapor and the complex plasma-vapor absorption characteristics make it challenging to model the vapor in a

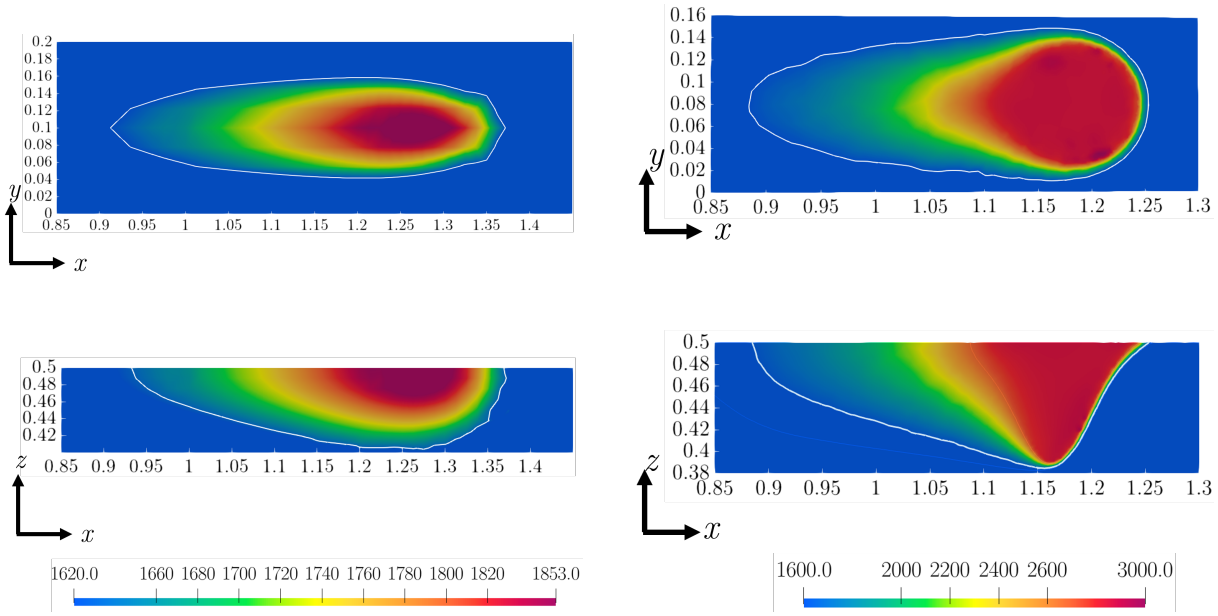

(a) Model presented here

(b) Model from project partners

Figure 10: The meltpool shape comparison for this papers' model with the model from project partners[58]

computationally efficient model (a much finer mesh is needed to accurately capture temperature variations within the vapor capillary). Their model was computationally more intensive as it simultaneously modelled the flow of potential on the meltpool surface as well as the evolution and movement of the meltpool surface itself. Still, the project partners have conducted their modelling using the same parameters as in Table 1 and it is feasible to compare meltpool dimensions to showcase the validity of the model presented in this research. The results of this comparison are shown in Fig. 10. For consistency, the meltpool length is measured as the maximum spatial extent in x direction, the width is the maximum spatial extent in the y direction and the depth is the maximum extent in z direction of the isotherm $T = T_{melt}$. Since, the model of the project partners (Ref. 58) uses two seperate meshes for modelling the complete meltpool, the second mesh, which actually encapsulated the liquid region, is what is directly comparible to the model presented here. For that region, the approximate meltpool width, depth and length that they reach is around 0.14 mm, 0.12 mm and 0.4 mm respectively. In contrast, with the model presented here, the generated meltpool is approximately 0.11mm wide, 0.1 mm deep and 0.44 mm long which is in reasonable agreement. It is understable, that even if the extents agree, the overall shape of the isotherm differs due to their model being more complex in terms of studying more detailed physics of the phase change, potential flow and dynamics of the meltpool but that is exactly why their model is computationally more demanding. Moreover, it is likely that with a finer mesh, the meltpool shape can be refined for the model described here.

Another study conducted by Ross *et al.*,[57] which focuses on accurate and quick calibrations of the heat source, has also been compared here in Fig. 11. They have published a thermal model after using an optimization technique to tune the heat source parameters to match experiments to their simulation results. The process parameters they use here are beam radius $r_b = 25\mu m$, laser power $P = 200W$, absorption factor $\eta = 0.73$ and scan speed $v = 700mm/s$, whereas they used SS316L material properties. These parameters and properties were also used to run the simulation with this papers' model. Single track models have been compared. Here, the authors from Ross *et al.* have visually clipped the maximum temperature to melting temperature, for clear visualization of the meltpool shape and boundaries, and thus the same is done for this papers' model. The meltpool is marked with a solid white line in both models to highlight its size and shape. The model from Ross *et al.* formed a meltpool with width $\approx 140\mu$m, depth $\approx 95\mu$m and length $\approx 480\ \mu$m. In comparison, the model presented here, generated a meltpool with width $\approx 110\mu$m, depth $\approx 90\mu$m and length $\approx 560\ \mu$m. Here, the current model overestimates the length somewhat but has good agreement in depth and width. This discrepancy

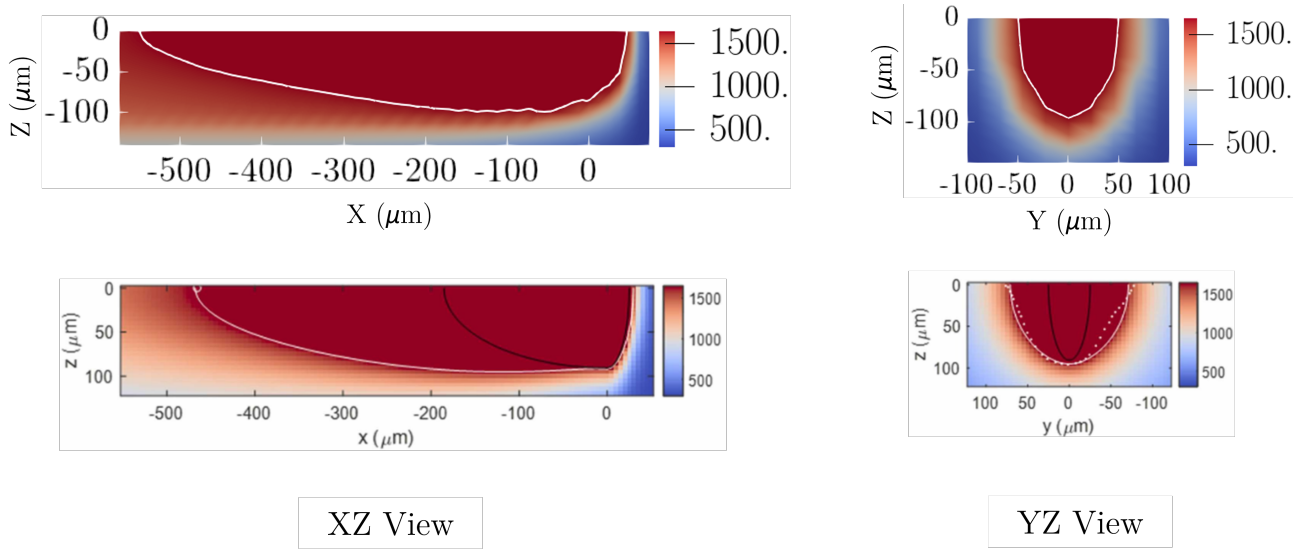

Figure 11: The meltpool shape and temporal distribution between this papers' model (top) and the model from Ross *et al.*(bottom). The solid white lines represent the computed meltpool boundaries for both models.

can also stem from the fact that Ross *et al.* used a different ratio between front and rear fractions of the heat source, to specifically minimise their heat source length to distribute more power to the front of the meltpool resulting in a better calibration of their heat source. However, even with an overestimated length, this papers' model better mimics the overall shape of the isosurface when compared with their model. The distortions in the white line for this papers' model are due to insufficient mesh resolution.

Next, the authors' compared their model with the model by Jonaet *et al.*[65] which was also a similar model albeit they used a combination of a Gaussian heat source for the heat flux in X and Y and a Lambert-Beer Law for the depth heat flux in Z direction respectively. Their model was implemented in the commercial COMSOL Multiphysics Modeling Software. Fine tuning the radii of the double ellipsoid heat source in this papers' model, the Goldak source could be shaped similar to their model. The choice of material this time was Ti6Al4V with absorption criteria taken from different experimental studies.[66,67] The key process parameters for this comparison are beam radius $r_b = 50\mu m$, laser power $P = 120W$, absorption factor $\eta = 0.75$ and scan speed $v = 1000mm/s$. This comparison could only be done for meltpool length and width (only top XY view) since the study by Jonaet *et al.* did simulations for a single layer and uses much longer tracks. The comparison is shown in Fig. 12. Here, the approximate width and length of the model from Jonaet *et al.* is 0.1 mm and 0.24 mm, whereas this papers' model predicted a meltpool width of 0.08mm and meltpool length of 0.2 mm respectively,

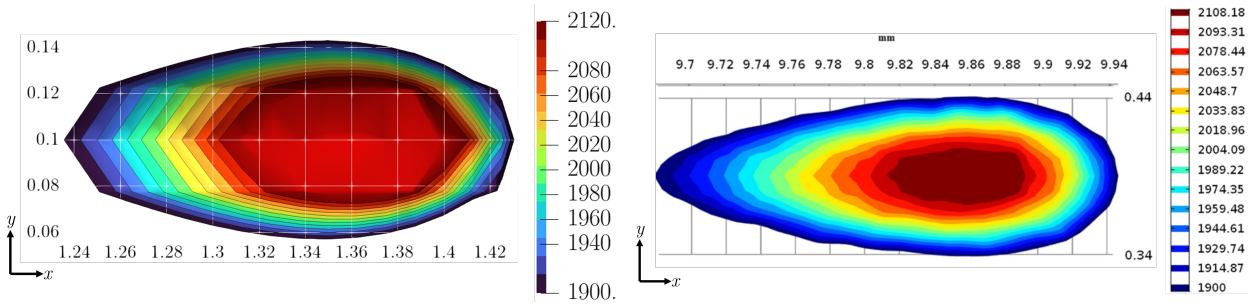

(a) Model presented here

(b) Model from Jonaet *et al.*

Figure 12: Temperature contours for isosurfaces of the meltpool for (a) this model and (b) the one presented by Jonaet *et al.*. Dimensions shown in mm for both images.

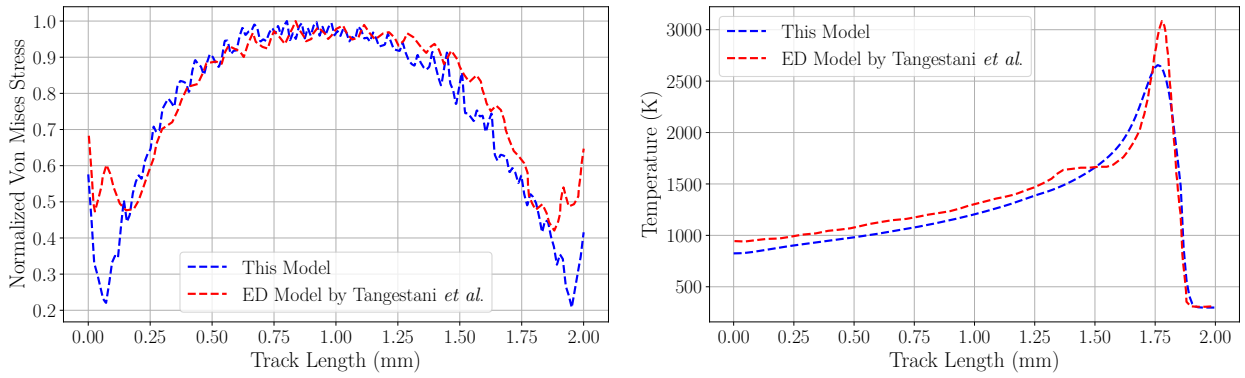

(a) (b)

Figure 13: The variation of (a) *normalized* von Mises stress vs track length and (b) temperature vs track length for this papers' model and model by Tangestani *et al.*

once again demonstrating good agreement with their model. The temperature distribution within the meltpool can also be illustrated as the contour-based variation matches very well with the model from Jonaet *et al.* and even the maximum temperature within the meltpool is comparable.

The authors were also able to locate a track level thermomechanical model by Tangestani *et al.*, to showcase an appropriate mechanical comparison. They have developed a track level model, which also accomodates the relative beam shift approach and is called a *hybrid-line* (HL) model.[21] They use ABAQUS® and a sequence of external subroutines to develop their single track models. The quantitative comparison for stress values was not possible directly due to different computational setup and differing geometry of track and domain (due to their meshing strategy). Nonetheless, the authors' were able to modify the model presented here to simulate their cooling and relaxation of BCs. This was done by explicitly defining a timestep (at the end of the track), where the heat source was turned off (set to zero) and then at another timestep, the new relaxed BCs were applied to the mechanical problem which was then solved from that timestep onwards. Hence, the Von Mises stress *variation* along the single track path could be compared. Since absolute values differed (due to the aformentioned discrepancies in meshing setup), a plot of normalized von Mises stress vs track length is shown. Additionally to showcase thermal validity, their thermal model was also compared for temperature along the track path (no normalization was not needed). Their plots have been digitized for raw data extraction using plot digitization tools.[68] This comparison is shown in Fig. 13. Their *ED* model is used since they use it as a baseline for accuracy test of their own model variations. The process parameters here were power $P = 200W$, absorption $\eta = 0.5$, scan velocity $v = 1000mm/s$ and beam radius $r_b = 60\mu m$. The material used is Nickel Super Alloy Rene 65™. The temperature comparison is done when the heat source has just passed 90% (1.8 mm) of the track length as per their work. Both plots show good agreement as the comparison illustrates but this papers' model underestimates the peak temperature reached which could be attributed to the different heat source shape used by Tangestani *et al.* They used an exponential decay for the depth direction of the heat flux whereas the model in this paper uses a Gaussian decay. The exponential decay results in a fast initial energy drop in the z-direction and thus (for the same total energy) the maximum energy flux, at the heat source center, is higher. Moreover, there is a certain *plateau* of Tangestani's model, as the temperature rises towards the location of the heat source, which could not be recreated with the model presented here. Aside from these discrepancies, the overall spatial variation and the temperature near the track starting point, are both well within reasonable margins. The stress comparison shows (as they also mentioned) that the stress is concentrated in the solidified regions and that the powder bed has no stress due to negligible stiffness, whereas not considering the stress-free status of the powder can lead to overestimation of stresses.[69] They also observed that the maximum stress occurs, in the center of track, where expansion and contraction are most constrained by surrounding material. Both they and the authors' obseved that the stress is lowest closest to the boundaries where the solidified material is free from constraints. Overall, the variation of stress has good agreement with their model.

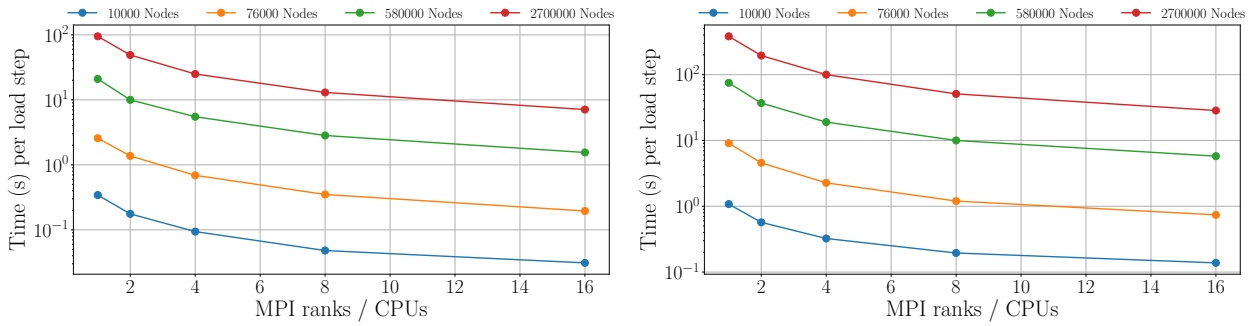

Figure 14: CPU walltimes for each load step for multiple CPUs at different mesh sizes

Proper calibration of the heat source is necessary to recreate unique meltpool shapes and temperature distributions for a valid model. This usually requires optimization and minimization approaches augmented into the model.[70,71] One such approach could be to incorporate machine learning models but that will require additional computational modelling effort to train the model.[72] To save time on recalibration requirements as the temperature changes during the process, the authors have also proposed an approach where a fixed temperature distribution (from a more detailed process model) can be used to mimic a *quasi-static* heat source for good approximation and reasonable computation times.[73] Another approach is to try a different heat source since some studies have shown that a heat source, with properly tailored combinations of an exponentially decaying depth function in conjuction with an in-plane Gaussian decay, can better reproduce temperatures for LPBF processes (fast moving source) compared to the traditional Goldak model, especially for thermally varying material properties.[74,75] Since the mechanical model is challenging to simulate with such fine detail for many individual tracks, researchers use an aggregrate/staggered approach to solve a full thermomechanical problem. In this case, the thermal history is allowed to accumulate for a large scale before a mechanical calculation step is conducted but this is then limited to larger scales thus restricting track level comparisons.

5.1.4 Computational efficiency

The model has been programmed in Python using DOLFINx/FENICs libraries for solving partial differential equations using the FEM. Therefore, these libraries take advantage of parallel processing techniques through the use of the Message Passing Interface (MPI).[44] Hence, the efficiency can be scaled by implementing the use of multiple processors as the degrees of freedom (DOFs) grow to maintain reasonable computational times. The computation times are calculated for one loadstep of the temperature increment i.e., thermal problem, and for the corresponding mechanical loadstep, which are shown in Fig. 14. As mentioned, the mechanical step is computationally more demanding than the thermal step. However with the model presented here, both steps gain equal computational advantage when the computation is split over multiple processors. For the largest mesh i.e. 270,000 Nodes, the thermal step requires around 100 seconds in single CPU performance and is accelerated upto more than 10 times when using 16 CPUs while the mechanical step requires around 500-600 seconds for single CPU and approximately $1/10^{\text{th}}$ of that when splitting over 16 CPUs.

Mesh resolution is a key factor in determining how much computational time is gained by using multiple processors.[44,76] This is because, increasing the number of CPUs also means additional computational overhead as all processors must communicate with each other as well. This leads to a stagnation in any computational time gained if this computational overhead becomes more costly than the savings gained from splitting the problem. Mesh resolution must also be considered in the regions of high temperature gradient. A dynamic/adaptive mesh refinement strategy is not yet implemented here but can serve to balance computational efficiency (coarse mesh in regions far away from the meltpool) with reasonable accuracy (finer mesh in regions close to and within the meltpool). Moreover, the mechanical problem is solved after every 5 thermal time steps, however since plastic deformation acrues in longer time and larger length scales (especially with cooldown and relaxation), the mechanical problem can be further accelerated by solving it after accumulation of even more thermal time steps of the thermal problem.[33,34]

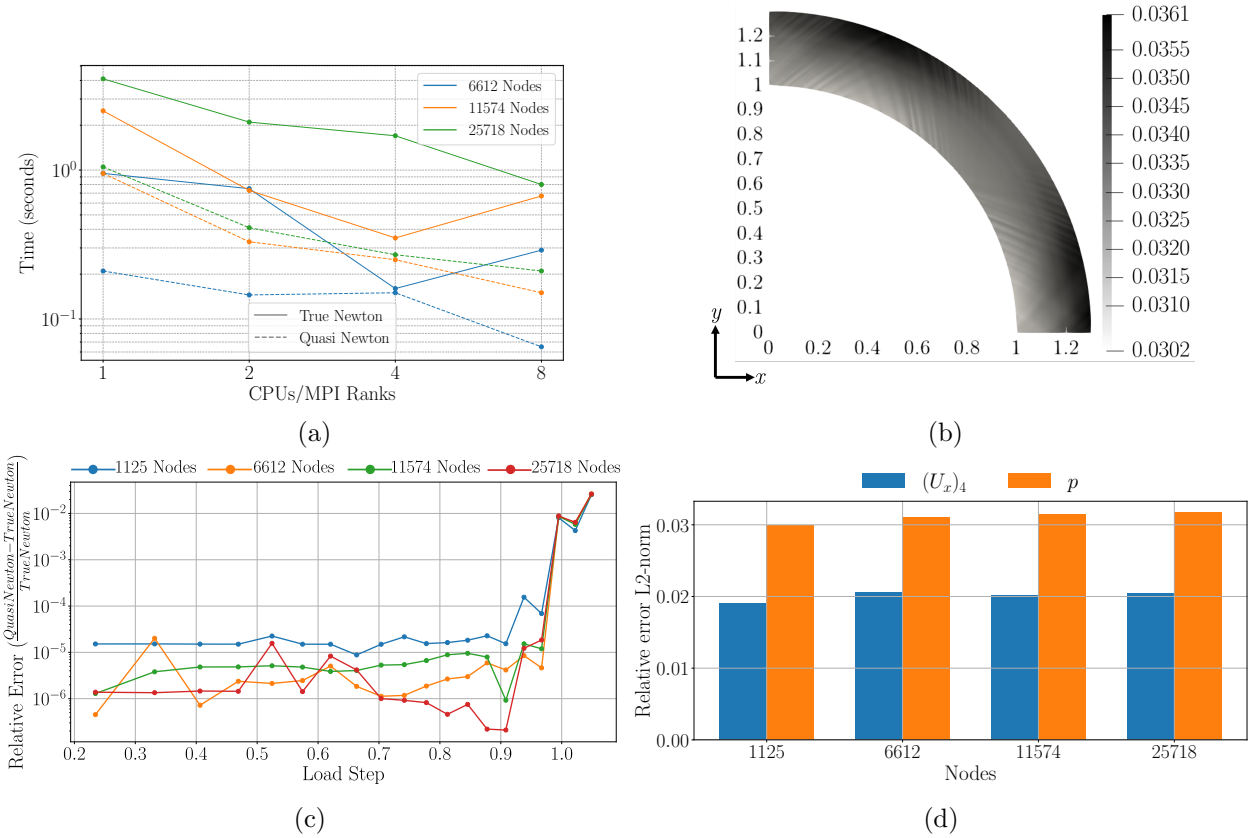

Figure 15: (a) A comparison of iteration times vs DOFs for both approaches (different colors represent DOFs while different line styles show which approach), (b) the relative error norm for the cumulative plastic strain over the domain, (c) the relative error of the X-displacement at Point 4 over all load steps and (d) the relative error norm for both X-displacement at Point 4 and cumulative plastic strain against increasing DOFs.

5.2 Mechanical model

To evaluate performance of the Quasi-Newton, the mechanical benchmark (showcased in Sec. 4.2) is a suitable small scale problem that can easily be manipulated for rapid parametric variations and is a well established benchmark for plasticity models. Performance gain is measured as the comparison for iteration time against degrees of freedom to showcase the relative cost of a True-Newton solve vs the Quasi-Newton solve as the system size increases or mesh is refined. Iteration time during the plastic deformation, which includes key load steps such as the start of plastic deformation and final load step, has been analyzed. For accuracy assessment, the relative error-difference between both approaches, for each load step/increment is studied using a pointwise comparison of the x-component of displacement, at inner radius vertex on the bottom horizonal edge (Point 4 of Fig. 3). Further accuracy checks are performed for the L^2 norm of the relative error of this displacement component. To evaluate the *global* accuracy, the L^2 norm of the relative error of the overall cumulative plastic strain p is also computed. To highlight stability,the comparison between both approaches is conducted over increasing DOFs. Additionally, the computational gains in both approaches upon using multi-processing are also highlighted to showcase that the Quasi-Newton's unchanging stiffness per iteration is a computational saving that gains from more processors.

Different results for iteration times, relative errors and mesh size stability have been illustrated in Fig. 15. In Fig. 15a, the computation times per iteration (during plastic deformation) is plotted for both Quasi-Newton and True-Newton approaches to showcase how both approaches scale with increased number of processors and how the Quasi-Newton approach also takes full advantage of the gains in matrix assembly and back solve with

more CPUs. Figure 15b showcases the overall relative error norm for the cumulative plastic strain p of the Quasi-Newton compared to True-Newton. In Fig. 15c, the relative error for X-displacement for each loadstep, is shown between both approaches and lastly, Fig. 15d shows how the relative error norms, for both the pointwise displacement and the overall cumulative plastic strain, vary with increasing DOFs, thus highlighting the stability of both approaches. Unlike the True-Newton where 8 CPUs become a limiting factor for computational time gained, the Quasi-Newton still scales well with that many CPUs and further gains computational speedup. This is because, as mentioned in Sec. 5.1.4, for the True-Newton additional CPUs demands more overhead than computational savings gained per extra CPU. On the other hand, splitting the problem up further among CPUs still results in a faster iteration time for the Quasi-Newton, as there is no additional effort for each CPU to invert the matrix, thus computational time is still gained even with that additional overhead. The Quasi-Newton approach also maintains reasonable error margins, compared with True-Newton, for pointwise ($< 5\%$) as well as global error norms ($< 4\%$), which also remain within reasonable margins at larger mesh sizes. Thus, larger matrix sizes do not introduce any additional stiffness or instability when using the Quasi-Newton approach. The point-wise displacement variations remain well below reasonable tolerances (10^{-5}) when the loadsteps are elastic and are still in acceptable margins during plastic deformation steps.

An expected disadvantage of treating the nonlinear (plastic) terms explicitly means the tangent stiffness matrix is not consistent anymore, but rather an approximation. This reduces the convergence of the Newton solve to linear (or superlinear with careful damping).[35] This leads to more iterations needed to reach convergence (based on tolerance threshold) even with a full recomputation for smaller residual norms. However, the iteration computation time itself is considerably reduced, since the tangent stiffness matrix is not reassembled and inverted in every time iteration of the Newton solve. Nevertheless, this approach uses Picard-style iterative approach which, although slower to converge, is not prone to divergence problems unlike the True Newton, which is susceptible to this based on the initial guess and might require additional stabilization especially for more complex elastoplastic laws, where the local constitutive update (stress correction) must also be computed as an iterative solve to a nonlinear problem.[77,78] Potential for overall improvement exists, when larger and larger DOFs are needed, since the gap between both approaches starts to narrow in terms of computation time for the whole problem as DOFs increase. This is because as the per iteration time for the True-Newton grows with larger DOFs, the total load step time for the True-Newton (which is a product of per iterations and number of iterations) will get closer and closer to the Quasi-Newton (which has more iterations but each iteration is faster) and eventually will get slower than the Quasi-Newton load step time when the DOFs get very large.

Thus, better overall performance is still possible for a thermomechanical model as well, considering the fact that the mechanical load step takes orders of magnitude longer to solve than the thermal increment calculation. Therefore, any benefit in the overall mechanical computation per thermal step is still beneficial, especially at larger scales where the mechanical calculation should be performed for every thermal step to ensure the displacement increment remains small enough for a stable convergence of the mechanical solver. Thus, as the degrees of freedom grow, as is the case with LPBF, the benefit of time saved per iteration should start to outweigh the disadvantage of slower convergence. Moreover, even if the tangent stiffness is now not algorithmically consistent, the drop in accuracy of the solution is not significant and is within acceptable tolerances. Nevertheless, further investigation is needed to see at which level of mesh size or DOFs does per iteration time for True-Newton gets large enough that it influences the load step (even if the number of iterations is less) to be slower than the equivalent load step time of Quasi-Newton.

6. CONCLUSION AND OUTLOOK

A computationally efficient, accurate and flexible thermomechanical model for the LPBF process has been presented in this research. Consideration to temperature dependent properties, nonlinear radiation boundary conditions as well as computationally valid heat sources has been incorporated into the thermal model. The mechanical model is coupled and incorporates plastic deformation and yielding with isotropic hardening. The approach focuses on making a an effective and accurate model for track level modelling of the moving laser beam. This is useful in keeping track of localized thermal and stress evolution to better study the localized buildup of plastic strains and can be further accelerated through the use of parallelization over multiple CPUs. Rapid development of computer hardware and accelerated computation on GPUs, can accelerate this model even further

for larger scales. Detailed validation has also been conducted with other relevant models in literature which have already been validated with experimental results. The model can be expanded to larger scales such that far-field temperature variations and mechanical deformations can be validated with larger scale thermomechanical models. Unfortunately, mechanical validation was difficult due to the lack of small scale track level mechanical models and thus expanding this model to larger scales will be the focus of subsequent investigations.

Additionally, to investigate acceleration of the nonlinear mechanical problem, a framework, titled the Quasi-Newton approach, is presented. It treats the incremental mechanical problem as an explicit problem of plasticity whereby the nonlinear plastic correction in the left hand side of the system is modelled as an explicit *plastic load* on the right hand side instead. To illustrate and investigate the computational benefits of this approach (over the standard fully implicit approach), a purely mechanical benchmark was investigated. The approach showcases per iteration speedup considerable but requires more iterations to reach a stable solution. While the effective use of multi-processing helps accelerate the Quasi-Newton approach, further investigation is needed to see at what scale of CPUs and DOFs is it a overall more effective approach than the classic True-Newton.

To circumvent the challenges of modelling the absorption and heat transer effects of vaporization and plasma generation, a simple absorption reduction model is implemented to limit laser beam power in vapor regions. This is coarse approximation and should be refined with an approximate exponential vapor flux law to better model the reduced absorption as well as deep penetration meltpools. The rapid heating and cooling cycles of the LPBF process are accompanied by cycles of yielding and unyielding, therefore a kinematic hardening term should also be incorporated into the yield criterion. More appropriate heat source models will also be a focus for future investigations. Cooling effects should also be modelled, as well as the analysis of more tracks to see how plastic strain accumulates. This will aid in developing an approximation strategy for multi-scale models that can transfer localized small scale information from such models to larger coarser models where the meshes are coarse and computational strategies can be made more efficient. This will allow for rapid re-runs and updates of the larger models but with improved fine scale information. Currently a strategy to actually track residual stresses is also being implemented which will dynamically change boundary conditions during the cool down phase to simulate part relaxation.

APPENDIX A. ALGORITHM FOR ELASTOPLASTIC COMPUTATION

To illustrate the complete process of solving the mechanical problem (including yield check, local stress correction and global tangent stiffness), Algorithm 1 showcases all the steps needed.

ACKNOWLEDGMENTS

Funded by the Deutsche Forschungsgemeinschaft (DFG, German Research Foundation) under Germany's Excellence Strategy – EXC-2023 Internet of Production – 390621612. This research is also funded by the Digital Photonic Production DPP Research Campus as part of the "Research Campus Public-Private Partnership for Innovation" research funding initiative of the German Federal Ministry of Education and Research (BMBF). As part of the German government's high-tech strategy, the BMBF is using this initiative to promote strategic and long-term cooperation between science and industry "under one roof"(Funding number: 13N15423).

REFERENCES

[1] Zhao, X. and Wang, T., "Laser powder bed fusion of powder material: A review," *3D. Print. Addit. Manuf.* **10**, 1439–1454 (Dec. 2023).

[2] Chowdhury, S., Yadaiah, N., Prakash, C., Ramakrishna, S., Dixit, S., Gupta, L. R., and Buddhi, D., "Laser powder bed fusion: a state-of-the-art review of the technology, materials, properties & defects, and numerical modelling," *J. Mater. Res. Technol.* **20**, 2109–2172 (2022).

[3] Puukko, P., Hepo-oja, L., Vatanen, S., Kaipainen, J., Mäkinen, M.-L., and Lindqvist, M., "Case study of the environmental impacts and benefits of a pbf-lb additively manufactured optimized filtrate nozzle," *Sci. Rep.* **14**, 22183 (Sep 2024).

[4] Liu, J. and Wen, P., "Metal vaporization and its influence during laser powder bed fusion process," *Mater. Des.* **215**, 110505 (2022).

Algorithm 1 Load-Step and Newton–Raphson Iteration for Thermo-Elasto-Plasticity[36]

Require: Displacement increment $\Delta\mathbf{u}_n$, plastic state $\{p_n, \boldsymbol{\sigma}_n\}$, temperature change ΔT, external loads $\{\mathbf{b}_{n+1}\}$
Ensure: Updated $\Delta\mathbf{u}_{n+1}$ and plastic state $\{p_{n+1}, \boldsymbol{\sigma}_{n+1}\}$

Initialize

$$\Delta\mathbf{u}^{(0)} \leftarrow \mathbf{0}, \quad \delta\mathbf{u}^{(0)} \leftarrow \mathbf{0}, \quad k \leftarrow 0$$

repeat maximum iterations reached or convergence

Compute trial strain

$$\Delta\boldsymbol{\varepsilon}_{\text{trial}} \leftarrow \varepsilon(\Delta\mathbf{u}_n) - \varepsilon^{\text{th}}(\Delta T)$$

Compute trial stress

$$\boldsymbol{\sigma}_{\text{trial}} \leftarrow \boldsymbol{\sigma}_n + \mathbb{C} : \Delta\boldsymbol{\varepsilon}_{\text{trial}}$$

Evaluate yield function

$$f \leftarrow \sqrt{\tfrac{3}{2}\,\|\text{dev}(\boldsymbol{\sigma}_{\text{trial}})\| : \|\text{dev}(\boldsymbol{\sigma}_{\text{trial}})\|} - \big(\sigma_{y0} + H\,p_n\big)$$

if $f < 0$ **then**

Elastic step:

$$\boldsymbol{\sigma}_{\text{proj}} \leftarrow \boldsymbol{\sigma}_{\text{trial}}, \quad \Delta p \leftarrow 0, \quad p_{\text{new}} \leftarrow p_n, \quad \mathbb{C}^{\text{p}} \leftarrow \mathbf{0}$$

else

Plastic return-mapping:

$$\{\boldsymbol{\sigma}_{\text{proj}},\ \tfrac{\partial f}{\partial \sigma_{\text{trial}}},\ \Delta p\} = \text{ReturnMap}\big(\Delta\boldsymbol{\varepsilon}_{\text{trial}},\ \{p_n, \sigma_n\}\big)$$

Update local variables:

$$p_{\text{new}} \leftarrow p_n + \Delta p, \quad \mathbb{C}^{\text{p}} \leftarrow \mathbb{C}^{\text{p}}\big(\tfrac{\partial f}{\partial \sigma_{\text{trial}}},\ \Delta p\big)$$

end if

Compute global residual

$$\mathbf{R}^{(k)} = \int_\Omega \mathbf{b}_{n+1}\cdot\delta\mathbf{u}\,d\Omega \;-\; \int_\Omega \sigma_{\text{proj}} : \varepsilon(\delta\mathbf{u})\,d\Omega$$

Compute tangent stiffness

$$\mathbf{K}^{(k)} = \int_\Omega \big(\mathbb{C} - \mathbb{C}^{\text{p}}\big) : \varepsilon(\boldsymbol{\phi}_j) : \varepsilon(\boldsymbol{\phi}_i)\,d\Omega$$

Solve for correction

$$\mathbf{K}^{(k)}\,\delta\mathbf{u}^{(k)} = -\,\mathbf{R}^{(k)}$$

Update increment

$$\Delta\mathbf{u}_n^{(k+1)} \leftarrow \Delta\mathbf{u}_n^{(k)} + \delta\mathbf{u}^{(k)}$$

if $\|\mathbf{R}^{(k)}\| < \text{tol}_{\text{NR}}$ **then**

break

else

$k \leftarrow k + 1$

end if

until convergence or k exceeds maximum

Finalize:

$$\mathbf{u}_{n+1} = \mathbf{u}_n + \Delta\mathbf{u}^{(k+1)}, \quad \{p_{n+1}, \boldsymbol{\sigma}_{n+1}\} = \{p_{\text{new}},\ \boldsymbol{\sigma}_{\text{proj}}\}.$$

[5] Zhao, C., Shi, B., Chen, S., Du, D., Sun, T., Simonds, B. J., Fezzaa, K., and Rollett, A. D., "Laser melting modes in metal powder bed fusion additive manufacturing," *Rev. Mod. Phys.* **94**, 045002 (Oct 2022).

[6] Li, C., Liu, Z., Fang, X., and Guo, Y., "Residual stress in metal additive manufacturing," *Procedia CIRP* **71**, 348–353 (2018). 4th CIRP Conference on Surface Integrity (CSI 2018).

[7] Wang, J., Zhu, R., Liu, Y., and Zhang, L., "Understanding melt pool characteristics in laser powder bed fusion: An overview of single- and multi-track melt pools for process optimization," *Advanced Powder Materials* **2**(4), 100137 (2023).

[8] Mostafaei, A., Ghiaasiaan, R., Ho, I.-T., Strayer, S., Chang, K.-C., Shamsaei, N., Shao, S., Paul, S., Yeh, A.-C., Tin, S., and To, A. C., "Additive manufacturing of nickel-based superalloys: A state-of-the-art review on process-structure-defect-property relationship," *Prog. Mater. Sci.* **136**, 101108 (2023).

[9] Cao, Y., Lin, X., Kang, N., Ma, L., Wei, L., Zheng, M., Yu, J., Peng, D., and Huang, W., "A novel high-efficient finite element analysis method of powder bed fusion additive manufacturing," *Addit. Manuf.* **46**, 102187 (2021).

[10] Ganeriwala, R., Strantza, M., King, W., Clausen, B., Phan, T., Levine, L., Brown, D., and Hodge, N., "Evaluation of a thermomechanical model for prediction of residual stress during laser powder bed fusion of ti-6al-4v," *Addit. Manuf.* **27**, 489–502 (2019).

[11] Peter, N., Pitts, Z., Thompson, S., and Saharan, A., "Benchmarking build simulation software for laser powder bed fusion of metals," *Addit. Manuf.* **36**, 101531 (2020).

[12] Romero-Hdz, J., Saha, B. N., Vallikavungal, J., and Zambrano-Robledo, P., "OpenAM-SimCCX: An Open-Source framework for Thermo-Mechanical analysis of additive manufacturing with CalculiX," *Materials* **18** (Oct. 2025).

[13] Huang, H., Wang, Y., Chen, J., and Feng, Z., "An efficient numerical model for predicting residual stress and strain in parts manufactured by laser powder bed fusion," *JPhys Mater.* **4**, 044006 (Oct. 2021).

[14] Soundararajan, B., Sofia, D., Barletta, D., and Poletto, M., "Review on modeling techniques for powder bed fusion processes based on physical principles," *Addit. Manuf.* **47**, 102336 (2021).

[15] Li, C., Liu, Z. Y., Fang, X. Y., and Guo, Y. B., "On the simulation scalability of predicting residual stress and distortion in selective laser melting," *J. Manuf. Sci. Eng.* **140**, 041013 (02 2018).

[16] Nickel, A., Barnett, D., and Prinz, F., "Thermal stresses and deposition patterns in layered manufacturing," *Mater. Sci. Eng. A* **317**(1), 59–64 (2001).

[17] Liang, X., Chen, Q., Cheng, L., Hayduke, D., and To, A. C., "Modified inherent strain method for efficient prediction of residual deformation in direct metal laser sintered components," *Comput. Mech.* **64**, 1719–1733 (Dec 2019).

[18] Liang, X., Cheng, L., Chen, Q., Yang, Q., and To, A. C., "A modified method for estimating inherent strains from detailed process simulation for fast residual distortion prediction of single-walled structures fabricated by directed energy deposition," *Addit. Manuf.* **23**, 471–486 (2018).

[19] Yuan, M. G. and Ueda, Y., "Prediction of residual stresses in welded t- and i-joints using inherent strains," *J. Eng. Mater. Technol.* **118**, 229–234 (04 1996).

[20] Bugatti, M. and Semeraro, Q., "Limitations of the inherent strain method in simulating powder bed fusion processes," *Addit. Manuf.* **23**, 329–346 (2018).

[21] Tangestani, R., Sabiston, T., Chakraborty, A., Yuan, L., Krutz, N., and Martin, É., "An efficient track-scale model for laser powder bed fusion additive manufacturing: Part 2—mechanical model," *Front. Mater.* **8** (Nov. 2021).

[22] Beneš, M. and Tichý, J., "On coupled navier—stokes and energy equations in exterior-like domains," *Comput. Math. Appl.* **70**(12), 2867–2882 (2015).

[23] Davalath, J. and Bayazitoglu, Y., "Forced convection cooling across rectangular blocks," *J. Heat Transf.* **109**, 321–328 (05 1987).

[24] Gan, G., "Impact of computational domain on the prediction of buoyancy-driven ventilation cooling," *Build. Environ.* **45**(5), 1173–1183 (2010).

[25] John A. Goldak, M. A., [*Computer Simulation of Welding Processes*], Springer, New York, NY, 1 ed. (2005).

[26] Fu, C. H. and Guo, Y. B., "Three-dimensional temperature gradient mechanism in selective laser melting of ti-6al-4v," *J. Manuf. Sci. Eng.* **136**, 061004 (10 2014).

[27] Goldak, J., Chakravarti, A., and Bibby, M., "A new finite element model for welding heat sources," *Metall. Mater. Trans. B* **15**, 299–305 (Jun 1984).

[28] Mises, R. v., "Mechanik der festen körper im plastisch- deformablen zustand," *Nachr. Ges. Wiss. Gottingen, Math.-Phys. Kl.* **1913**, 582–592 (1913). (in German).

[29] Simo, J. and Hughes, T., [*Computational Inelasticity*], Springer New York, NY, New York, NY, 21 ed. (1998).

[30] Lemaitre, J. and Chaboche, J.-L., [*Mechanics of Solid Materials*], ch. 5, 161–252, Cambridge University Press (1990).

[31] Brenner, S. C. and Scott, L. R., [*Polynomial Approximation Theory in Sobolev Spaces*], 93–127, Springer New York, New York, NY (2008).

[32] Masoomi, M., Soltani, A., Shamsaei, N., and Thompson, S., "Convection heat transfer coefficients for laser powder bed fusion," in [*Proceedings of the 29th Annual International Solid Freeform Fabrication Symposium*], 1686–1693, University of Texas at Austin (11 2018).

[33] Armero, F. and Simo, J. C., "A new unconditionally stable fractional step method for non-linear coupled thermomechanical problems," *Int. J. Numer. Methods Eng.* **35**(4), 737–766 (1992).

[34] Danowski, C., Gravemeier, V., Yoshihara, L., and Wall, W. A., "A monolithic computational approach to thermo-structure interaction," *Int. J. Numer. Methods Eng.* **95**(13), 1053–1078 (2013).

[35] Simo, J. and Taylor, R., "Consistent tangent operators for rate-independent elastoplasticity," *Comput. Methods Appl. Mech. Eng.* **48**(1), 101–118 (1985).

[36] Logg, A., Mardal, K.-A., and Wells, G., [*Automated Solution of Differential Equations by the Finite Element Method*], Springer (2012).

[37] Crank, J. and Nicolson, P., "A practical method for numerical evaluation of solutions of partial differential equations of the heat-conduction type," *Math. Proc. Camb. Philos. Soc.* **43**(1), 50–67 (1947).

[38] Courant, R., Friedrichs, K., and Lewy, H., "Über die partiellen differenzengleichungen der mathematischen physik," *Math. Annal.* **100**, 32–74 (1928). (in German).

[39] Bonnet, M., Frangi, A., and Rey, C., [*The finite element method in solid mechanics*], McGraw Hill Education (2014).

[40] de Souza Neto, E. A., Perić, D., and Owen, D., [*Finite Elements in Small-Strain Plasticity Problems*], ch. 7, 191–263, John Wiley and Sons, Ltd (2008).

[41] Wilkins, M. L., "CALCULATION OF ELASTIC-PLASTIC FLOW," Tech. Rep. UCRL-7322, Lawrence Radiation Laboratory, University of California, Livermore, CA (Apr. 1963).

[42] Logg, A. and Wells, G. N., "Dolfin: Automated finite element computing," *ACM Trans. Math. Softw.* **37**, 20:1 (Apr. 2010).

[43] Alnæs, M. S., Logg, A., Ølgaard, K. B., Rognes, M. E., and Wells, G. N., "Unified form language: A domain-specific language for weak formulations of partial differential equations," *ACM Trans. Math. Softw.* **40**(2), 9:1 (2014).

[44] Balaji, P., Buntinas, D., Goodell, D., Gropp, W., Kumar, S., Lusk, E., Thakur, R., and Träff, J. L., "Mpi on a million processors," in [*19th European MPI Users' Group Meeting*], Ropo, M., Westerholm, J., and Dongarra, J., eds., 20–30, Springer Berlin Heidelberg, Berlin, Heidelberg (2009).

[45] Řehoř, M. and Hale, J. S., "FEniCSx-pctools: Tools for PETSc block linear algebra preconditioning in FEniCSx," *J. Open Res. Softw.* **13** (Sept. 2025).

[46] Dalcin, L. D., Paz, R. R., Kler, P. A., and Cosimo, A., "Parallel distributed computing using python," *Adv. Water Resour.* **34**(9), 1124–1139 (2011).

[47] Patil, N., Ganeriwala, R., Solberg, J. M., Hodge, N. E., and Ferencz, R. M., "Benchmark multi-layer simulations for residual stresses and deformation in small additively manufactured metal parts," *Addit. Manuf.* **45**, 102015 (2021).

[48] Vasilyeva, M., Ammosov, D., and Vasil'ev, V., "Finite element simulation of thermo-mechanical model with phase change," *Computation* **9**(1) (2021).

[49] Koric, S., Hibbeler, L. C., and Thomas, B. G., "Explicit coupled thermo-mechanical finite element model of steel solidification," *Int. J. Numer. Methods Eng.* **78**(1), 1–31 (2009).

[50] Lu, D., Zhou, X., Liang, J., and Du, X., [*Stress Update Algorithm Based on Numerical Differentiation Methods*], 223–252, Springer Nature Singapore, Singapore (2025).
[51] Bathe, K.-J., [*Finite element procedures*], Klaus-Jurgen Bathe (2006).
[52] Famiyesin, O., "Energy adaptation of non-associated plasticity tangent matrices for symmetric solvers," *Comput. Struct.* **79**(13), 1233–1250 (2001).
[53] Atkinson, K. E., [*An introduction to numerical analysis*], Wiley, 2 ed. (1991).
[54] Picard, E., "Mémoire sur la théorie des équations aux dérivées partielles et la méthode des approximations successives," *J. Math. Pures Appl.* **6**, 145–210 (1890).
[55] KoŁodziej, J. A. and Gorzelańczyk, P., "Application of method of fundamental solutions for elasto-plastic torsion of prismatic rods," *Eng. Anal. Bound. Elem.* **36**(2), 81–86 (2012).
[56] Quarteroni, A., Sacco, R., and Saleri, F., [*Nonlinear Systems and Numerical Optimization*], 285–331, Springer Berlin Heidelberg, Berlin, Heidelberg (2007).
[57] Ross, A., Bitharas, I., Perkins, K., and Moore, A., "Volumetric heat source calibration for laser powder bed fusion," *Addit. Manuf.* **60**, 103267 (2022).
[58] Zielinski, J., *A holistic approach to understand laser additive manufacturing from melt pool to microstructure*, phd thesis, RWTH Aachen University, Aachen, Germany (July 2022).
[59] Pottlacher, G., Hosaeus, H., Wilthan, B., Kaschnitz, E., and Seifter, A., "Thermophysikalische eigenschaften von festem und flüssigem inconel 718," *Thermochim. Acta* **382**(1), 255–267 (2002). (in German).
[60] Han, J. and Wright, L., [*Analytical Heat Transfer*], CRC Press, Boca Raton, FL, 2 ed. (2022).
[61] Bleyer, J., Latyshev, A., and Maurini, C., "Numerical Tours of Computational Mechanics with FEniCSx." 29 January 2024, https://bleyerj.github.io/comet-fenicsx/tours/nonlinear_problems/plasticity/plasticity.html/ (2024). (Accessed: 20 September 2024).
[62] Crossland, B., Jorgensen, S. M., and Bones, J. A., "The strength of thick-walled cylinders," *J. Manuf. Sci. Eng. (ASME)* **81**(2), 95–111 (1959).
[63] Lin, S., Gan, Z., Yan, J., and Wagner, G. J., "A conservative level set method on unstructured meshes for modeling multiphase thermo-fluid flow in additive manufacturing processes," *Comput. Methods Appl. Mech. Eng.* **372**, 113348 (2020).
[64] Hecht, F., "New development in freefem++," *J. Numer. Math.* **20**(3-4), 251–265 (2012).
[65] Jonaet, A., Park, H. S., and Myung, L. C., "Prediction of residual stress and deformation based on the temperature distribution in 3d-printed parts," *Int. J. Adv. Manuf. Tech.* **113**, 2227–2242 (Apr. 2021).
[66] Rubenchik, A., Wu, S., Mitchell, S., Golosker, I., LeBlanc, M., and Peterson, N., "Direct measurements of temperature-dependent laser absorptivity of metal powders," *Appl. Opt.* **54**, 7230–7233 (Aug 2015).
[67] Boley, C. D., Mitchell, S. C., Rubenchik, A. M., and Wu, S. S. Q., "Metal powder absorptivity: modeling and experiment," *Appl. Opt.* **55**, 6496–6500 (Aug 2016).
[68] Rohatgi, A., "WebPlotDigitizer (5.2)." https://automeris.io/ (2011). [Computer software].
[69] Irwin, J. and Michaleris, P., "A line heat input model for additive manufacturing," *J. Manuf. Sci. Eng. Trans. (ASME)* **138**, 111004 (06 2016).
[70] Chen, C., Lin, Y.-J., Ou, H., and Wang, Y., "Study of heat source calibration and modelling for laser welding process," *Int. J. Precis. Eng. Manuf.* **19**, 1239–1244 (Aug 2018).
[71] Chen, C., Zhou, J., Zhao, T., Lian, G., and Huang, X., "Correlating laser additive manufacturing process with heat source coefficients by integrated experimental and numerical models," *3D Print. Addit. Manuf.* **12**(4), 343–364 (2025).
[72] Kusano, M. and Watanabe, M., "Heat source model development for thermal analysis of laser powder bed fusion using bayesian optimization and machine learning," *Integr. Mater. Manuf. Innov.* **13**, 288–304 (Mar 2024).
[73] Usman, K., Kruse, H., Niessen, M., Schleifenbaum, J., and Schulz, W., "A novel modelling approach for simulating meltpool movement in laser-based additive manufacturing," *J. Laser Micro/Nanoeng* **20**(1), 22–34 (2025).
[74] Liu, S., Zhu, H., Peng, G., Yin, J., and Zeng, X., "Microstructure prediction of selective laser melting alsi10mg using finite element analysis," *Mater. Des.* **142**, 319–328 (2018).

[75] Zhang, Z., Huang, Y., Rani Kasinathan, A., Imani Shahabad, S., Ali, U., Mahmoodkhani, Y., and Toyserkani, E., "3-dimensional heat transfer modeling for laser powder-bed fusion additive manufacturing with volumetric heat sources based on varied thermal conductivity and absorptivity," *Opt. Laser Technol.* **109**, 297–312 (2019).

[76] Gustafson, J. L., "Reevaluating amdahl's law," *Commun. ACM* **31**, 532–533 (May 1988).

[77] Yarushina, V. M., Dabrowski, M., and Podladchikov, Y. Y., "An analytical benchmark with combined pressure and shear loading for elastoplastic numerical models," *Geochem. Geophys. Geosystems* **11**(8) (2010).

[78] Strniša, F., Jančič, M., and Kosec, G., "Numerical analysis of small-strain elasto-plastic deformation using local radial basis function approximation with picard iteration," *Appl. Math. Model.* **137**, 115714 (2025).